PNAS RESEARCH ARTICLE | BIOPHYSICS AND COMPUTATIONAL BIOLOGY OPEN ACCESS

Engineered molecular sensors for quantifying cell surface crowding

Sho C. Takatori[a,b,1,2], Sungmin Son[a,c,1,2], Daniel S. W. Lee[a], and Daniel A. Fletcher[a,d,e,f,2]

Edited by Jennifer Lippincott-Schwartz, Janelia Farm Research Campus, Ashburn, VA; received November 19, 2022; accepted April 13, 2023

Cells mediate interactions with the extracellular environment through a crowded assembly of transmembrane proteins, glycoproteins and glycolipids on their plasma membrane. The extent to which surface crowding modulates the biophysical interactions of ligands, receptors, and other macromolecules is poorly understood due to the lack of methods to quantify surface crowding on native cell membranes. In this work, we demonstrate that physical crowding on reconstituted membranes and live cell surfaces attenuates the effective binding affinity of macromolecules such as IgG antibodies in a surface crowding-dependent manner. We combine experiment and simulation to design a crowding sensor based on this principle that provides a quantitative readout of cell surface crowding. Our measurements reveal that surface crowding decreases IgG antibody binding by 2 to 20 fold in live cells compared to a bare membrane surface. Our sensors show that sialic acid, a negatively charged monosaccharide, contributes disproportionately to red blood cell surface crowding via electrostatic repulsion, despite occupying only ~1% of the total cell membrane by mass. We also observe significant differences in surface crowding for different cell types and find that expression of single oncogenes can both increase and decrease crowding, suggesting that surface crowding may be an indicator of both cell type and state. Our high-throughput, single-cell measurement of cell surface crowding may be combined with functional assays to enable further biophysical dissection of the cell surfaceome.

cell surface crowding | cancer cell biology | glycocalyx | biophysics | plasma membrane

Significance

Cells interact with each other and the extracellular environment through a crowded assembly of polymers on their plasma membranes. The high density of these surface polymers can generate physical crowding that impacts cell function. However, tools to quantify the extent and effect of surface crowding on live cell membranes are lacking. In this work, we design macromolecular sensors that act as reporters of cell surface crowding. We combine experiments on reconstituted and live cell surfaces with molecular dynamics simulations to provide a mechanistic understanding of how cell surface crowding reduces binding of soluble molecules, and we show that crowding varies significantly with cell type and is affected by oncogene expression.

The biophysical organization of proteins, glycoproteins, and glycolipids that densely coat the surface of the cell membrane has been shown to govern many important physiological processes. Physical crowding on cell surfaces has a connection to cancer malignancy (1–3), and the dense glycocalyx on cancer cell surfaces can sterically hinder antibody binding and phagocytosis by immune cells (4). Recent studies have shown that the glycocalyx can also attenuate the binding of viruses and lectins to cell surface receptors (5–7). Surface crowding also alters protein mobility and sorting (8), as well as membrane channel gating (9). However, quantitative methods to obtain a detailed, mechanistic understanding of plasma membrane density and the biophysical interactions that govern macromolecular binding on live cell surfaces are lacking. This leaves basic questions about cell surface crowding unanswered, including the extent to which glycosylation contributes, how crowding differs among cell types and states, and even how best to quantify crowding in live cells.

While proteomic analysis of cell surface proteins provide detailed information on the relative abundance of proteins at the population level (10), it is difficult to predict collective biophysical features of cell surfaces simply from knowledge of the surface proteome. Previous studies have shown that the physical accessibility of large soluble ligands and macromolecules decreases on synthetic surfaces grafted with synthetic polymers or purified proteins (11–14). Other studies have developed tools that measure effects of surface crowding, including Houser et al. (15), who measured the separation of Förster resonance energy transfer pairs as a function of the steric interactions within the surface polymers on reconstituted membranes, and Son et al. (16), who measured nanometer-scale changes in height of multidomain proteins in vitro as surface density increased. While these studies of reconstituted systems provide valuable insights, direct quantification of surface crowding on live cell membranes remains a challenge. Advanced imaging techniques like electron microscopy enable nanometer-scale visualization of the cell membrane (17), but the preparation process is destructive, and structural information does not easily translate to a physical understanding of the effects of crowding, leaving a need for new tools to study the surfaces of living cells (3).

Here, we report a simple approach to measure surface crowding on live cells. Inspired by theoretical work on the adsorption of macromolecules on crowded surfaces (18), we engineered macromolecular probes that insert into bilayer membranes and quantify the repulsive penalty posed by crowded cell surfaces by a reduction in effective affinity. We first validated

Author contributions: S.C.T., S.S., and D.A.F. designed research; S.C.T., S.S., and D.S.W.L. performed research; S.C.T., S.S., and D.S.W.L. analyzed data; and S.C.T., S.S., D.S.W.L., and D.A.F. wrote the paper.

The authors declare no competing interest.

This article is a PNAS Direct Submission.

[1]S.C.T. and S.S. contributed equally to this work.

[2]To whom correspondence may be addressed. Email: stakatori@ucsb.edu, smson@kaist.ac.kr, or fletch@berkeley.edu.

This article contains supporting information online at https://www.pnas.org/lookup/suppl/doi:10.1073/pnas.2219778120/-/DCSupplemental.

Published May 15, 2023.

the measurement principle by engineering polymer–cholesterol conjugates of varying sizes and measuring their effective binding affinity on reconstituted membranes and red blood cell (RBC) membranes. We quantified the reduction in binding affinity as a crowding energy using molecular dynamics (MD) simulations and adsorption theories. We then engineered a two-component sensor based on the binding of a monoclonal anti-biotin antibody to a biotin–fluorophore–cholesterol conjugate that inserts into live cell plasma membranes. By measuring the fraction of antibody bound to the surface biotin on individual cells relative to bare model membranes, we quantify the effect of cell surface crowding on antibody-binding affinity. Our crowding sensors work on cells of different size, shape, and membrane lipid compositions, providing a technique to compare surface crowding across different live cell types and states.

Results

Physical Crowding on Membrane Surfaces Reduces the Binding Affinity of Soluble Macromolecules. Existing theories of adsorption thermodynamics give a direct relationship between the dissociation constant of a soluble macromolecule and the free energy of the surface, $K_D = \exp(U/(k_BT))$ (Fig. 1*A*). Therefore, a measurement of the K_D on a surface is a reporter of its free energy. By measuring the dissociation constants on a crowded surface, K_D, and a bare surface, K_D^0, we can measure the energy penalty posed by surface crowding, $\Delta U = k_BT \ln (K_D/K_D^0)$. To test whether we could use this principle to read out surface crowding, we conducted coarse-grained MD simulations to study the binding of macromolecules to a bare surface and to a surface decorated with polymers (Fig. 1*A*). We found that the free energy as a function of distance from the surface increases in the presence of surface-tethered polymers (Fig. 1*B*), and the deviation of the energy minima is a direct readout of the effective dissociation constant, K_D (see *SI Appendix* for further detail). We plot all results as a ratio of K_D/K_D^0, since the crowding energy is given by $\Delta U = k_BT \ln (K_D/K_D^0)$and only relative differences are important for surface crowding. As expected, we find that K_D/K_D^0 increases as we increase the surface crowding by changing either the surface density or the contour length of the crowding polymers (Fig. 1*C*). It is important to note that the contour length of the surface polymers has a strong effect on K_D, which demonstrates that the polymer number density alone is an insufficient metric of surface crowding.

Guided by these predictions, we engineered a series of exogenous macromolecular probes with known size and affinity to a lipid bilayer by conjugating cholesterol and fluorescent dyes to PEG 1k, dextran 10k, and dextran 40k macromolecules (Fig. 1*D* and *Materials and Methods*). The diameters of these probes are approximately 2, 4, and 10 nm based on the radii of gyration (19). We hypothesized that the reduced binding affinities of these "crowding sensors" to crowded membrane surfaces would act as a reporter of the energy penalty posed by surface crowding. We first tested the binding of our sensors to a supported lipid bilayer (SLB) formed on a glass bead and decorated it with PEG3k polymers simulating cell surface crowding. After allowing the sensor binding to reach equilibrium (45 min), we quantified the bead fluorescence with a flow cytometer. Using an adsorption isotherm to relate the bound sensor concentration to the bulk concentration, we calculated the effective dissociation constant. We found that the K_D of the larger dextran 10k and 40k sensors increased on the PEG3k surface compared to that on the bare surface, with the K_D of the dextran 40k sensor increasing by 55% when the SLB contained 1% (mol/mol) PEG3k (~15,000/μm^2 area density) (Fig. 1*E*), which agrees with our simulation and is consistent with previous studies (12). In contrast, the small PEG 0.5k sensor experienced no change in K_D for the PEG3k surface densities we tested (Fig. 1*E*). We observed no systematic change in the time to reach equilibrium on crowded surfaces compared to bare surfaces (*SI Appendix*).

To test the sensors' ability to read out crowding due to proteins rather than synthetic PEG polymers, we then reconstituted SLBs with engineered proteins based on repeats of the FNIII domain, Fibcon, which has a size of ~4 nm per domain (20). We used different lengths based on one (Fib1L), three (Fib3L), or five (Fib5L) domain proteins with decahistidine tags that bind to SLBs containing 1,2-dioleoyl-sn-glycero-3-(N-(5-amino-1-carboxypentyl) iminodiacetic acid)succinyl (DGS-Ni-NTA). The K_D of the dextran 40k sensor increased by more than 2× on surfaces crowded with Fib3L and Fib5L at a density of ~10,000/μm^2 relative to a bare membrane, whereas the K_D increased by only ~20% for Fib1L (Fig. 1*F*). It is important to note that the molecular weight of Fib1L (~14 kDa) is 4.6 times larger than PEG3k, yet the crowding strength generated by the PEG surface is 25% larger when comparing them at the same number density. These results highlight the fact that the molecular weight of a surface species is not a proper metric of crowding, just as number density and height of surface species are insufficient metrics by themselves. Indeed, "crowding" as it affects the affinity of soluble molecules at the cell surface is a collective phenomenon that includes these and other cell surface molecular properties.

Our simulations and reconstituted SLB experiments demonstrate the connection between surface crowding and effective binding affinities of large macromolecules. Our simple measurement of K_D is a quantitative reporter of surface crowding, regardless of the chemical identity of the surface species. The sensitivity of our sensors to protein length, molecular weight, and density provides a unique approach for studying the biophysical organization of the cell surface.

Macromolecular Binding at Cell Surfaces Is Osmotically Regulated by Sialylation. We next used the crowding sensors to study the effects of glycosylation on crowding on both reconstituted membranes and live plasma membranes. We reconstituted SLBs decorated with purified Glycophorin A (GYPA), a mucin-like transmembrane protein with a heavily glycosylated and sialylated extracellular domain (21). We found that the effective K_D of our dextran 40k sensor increased by 2× on the crowded GYPA surface compared to a bare membrane (Fig. 2*A*). When we treated the GYPA-coated beads with sialidase from *Clostridium perfringens* (*Clostridium welchii*), we found that the removal of sialic acid, a negatively charged monosaccharide, decreased K_D by 40% compared to the untreated GYPA surfaces. We hypothesized that the negative charge on sialic acids stiffens and stretches the disordered GYPA chain due to intrachain electrostatic repulsion, effectively increasing its persistence length and posing a larger energetic penalty against sensor binding at the surface. Polymer chain stiffening due to electrostatic interactions causes both the osmotic pressure and the effective volume of the polyelectrolyte surface brush to increase, leading to larger K_D (see *SI Appendix* for the relationship between K_D, osmotic pressure, and glycocalyx volume). GYPA contains 30 sialic acids held in close proximity (≈ 1 nm) in its 15 O-glycans (21), resulting in a large negative charge density along its disordered chain. For end-grafted polymer brushes, strong repulsion among the polymer side chains acts to stiffen the polymers and increase the overall height of the brush (22). We note that interchain interactions would also increase the brush height,

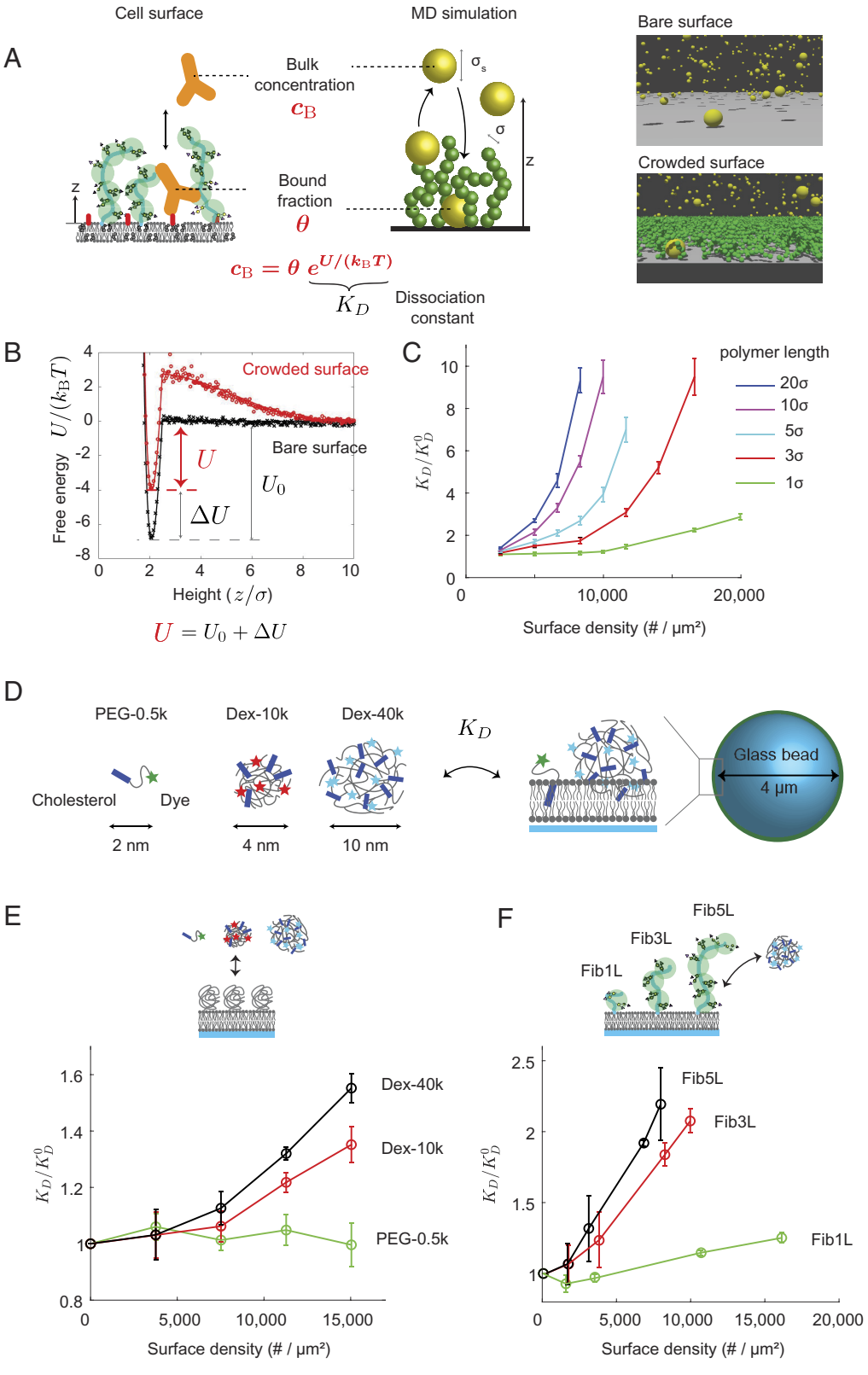

Fig. 1. Macromolecular binding is a reporter of surface crowding. (*A*) Soluble macromolecules, like monoclonal antibodies, experience a repulsive energy penalty when binding to antigen targets located on crowded surfaces. Therefore, the concentration of surface-bound macromolecules is a direct readout of the effective dissociation constant and the crowding state of the surface. (*Right*) Snapshots of coarse-grained molecular dynamics (MD) simulations on bare and crowded surfaces. Soluble macromolecules (yellow spheres) of size σ_s bind onto a surface functionalized with multidomain protein polymers (green spheres) with density, n, and monomer size, σ. (*B*) MD simulations are used to calculate the binding energy of soluble macromolecules on bare (black symbols) and crowded (red symbols) surfaces. The binding affinity of soluble macromolecules on crowded surfaces (U) is smaller than that on bare surfaces (U_0). The difference, $\Delta U = U - U_0$, is related to the crowding-induced change in the effective dissociation constant, K_D. Polymer brush theories are used to relate the effective dissociation constant to surface crowding (solid curves). See *SI Appendix* for further theoretical and computational results. (*C*) The dissociation constant, K_D, normalized by the bare-surface value, K_D^0, increases monotonically with the surface protein density and contour length. (*D*) Experimental design of cholesterol-based sensors to measure crowding on membranes. Synthetic polymers of different molecular weights are used to vary the overall size of the sensor. The sensors have a strong binding affinity to the lipid bilayer, and fluorescent labels provide a readout of bound surface concentration and the effective dissociation constant, K_D. (*E*) Normalized dissociation constant, K_D/K_D^0, of the small (PEG-0.5k), medium (Dex-10k), and large (Dex-40k) sensors increases on lipid-coated beads functionalized with PEG-3k at varying surface densities. K_D^0 is the affinity on bare lipid-coated beads. (*F*) K_D/K_D^0 of large Dex-40k sensors increases on lipid-coated beads functionalized with engineered proteins of the FNIII domain repeats, Fibcon (Fib), which has a size of ~4 nm per domain. Fib1L, Fib3L, and Fib5L contain 1, 3, and 5 domains, respectively. For all data, error bars indicate SDs of the mean; N > 3.

but are likely playing a minor role due to screening of charges in physiological buffers. The average spacing between grafting sites of GYPA chains is ≈20 nm at 2,000/μm^2 surface density, which is 30× larger than the 0.7-nm Debye length in physiological buffers (length scale over which charge interactions are screened).

To study the extent of crowding posed by sialylation on live cell membranes, we examined human RBC membranes, where the average protein compositions and copy numbers are well characterized (21, 23). Approximately 23% of the RBC membrane surface area is occupied by proteins (24), with GYPA and Band 3 being two of the bulkiest and most abundant proteins. Given that GYPA contains 75% of the total sialic acids on RBCs, and because one-third to one-half of sugars on its 15 O-glycans are sialic acids (21), we hypothesized that GYPA plays a major role in mediating RBC surface crowding. Anionic transporter Band 3 is a multipass transmembrane protein with a single extracellular N-glycan with

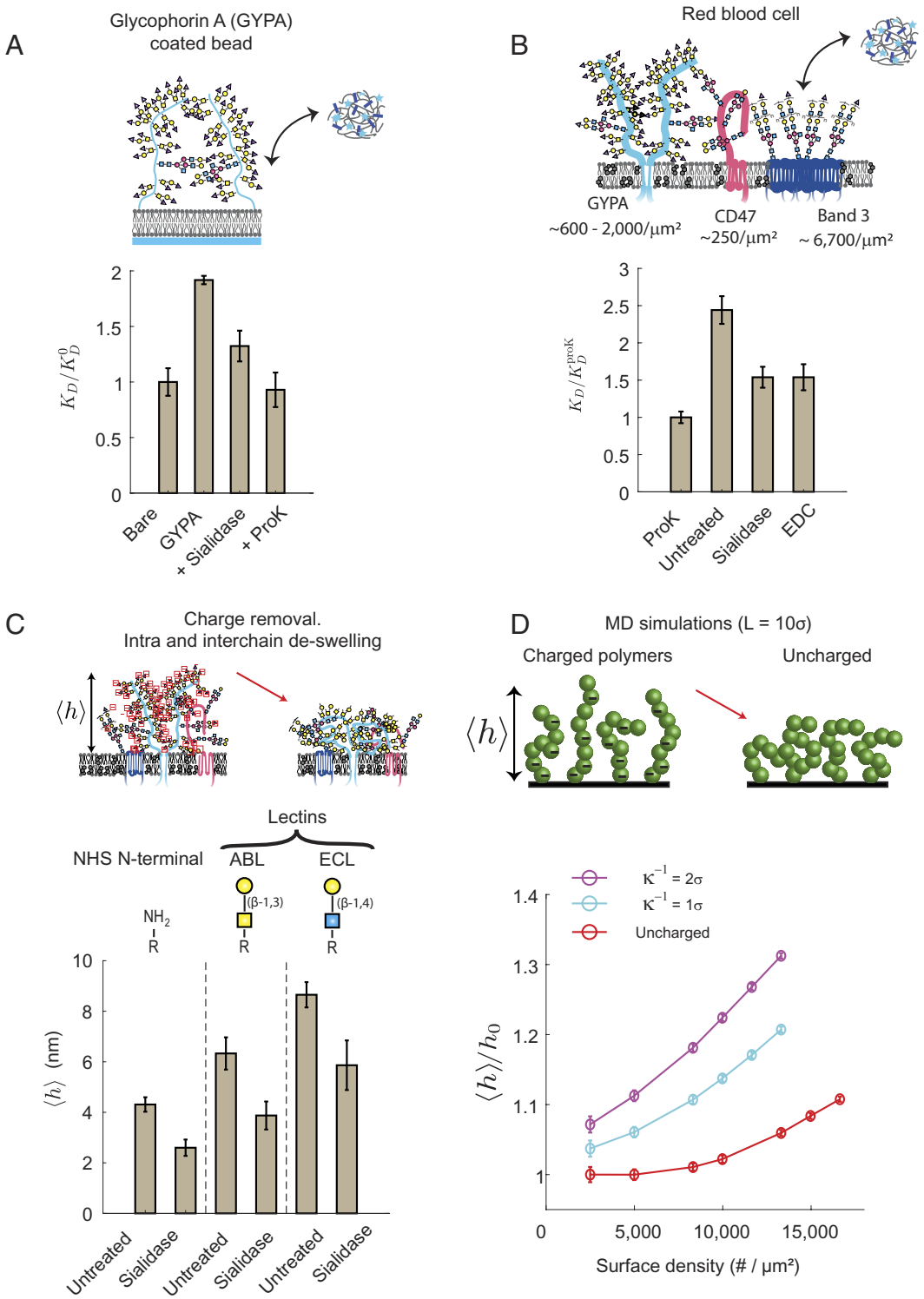

Fig. 2. Macromolecular binding on red blood cell (RBC) surfaces is osmotically regulated by sialylation. (*A*) Normalized dissociation constant of the large Dex-40k sensors, K_D/K_D^0, on reconstituted membranes with Glycophorin A (GYPA), a mucin-like glycoprotein found on RBCs. Treatment of the GYPA-bound beads with sialidase removes the sialic acids, which deswells the GYPA and increases the surface accessibility for the sensor. Proteinase K (ProK) removes GYPA and the affinity is restored to the same value as bare beads. (*B*) Dissociation constant of large Dex-40k sensors on RBCs, normalized by the affinity on ProK-treated cells, K_D^{proK}. Sialidase treatment removes the sialic acids on the RBC surface and decreases K_D, consistent with the results on GYPA-bound beads. EDC carbodiimide chemistry removes the negative charge on the RBC surface. The K_D reduction is the same as that with sialidase treatment, consistent with our hypothesis that electrostatic charge repulsion within the glycocalyx reduces the accessibility of the sensors. Note that the affinities are normalized relative to the ProK-treated cells, K_D^{proK}, which is different from the baseline on bare lipid-coated beads, K_D^0. (*C*) Average height of the RBC surface proteins, $\langle h \rangle$, is measured in an untreated cell and cells treated with sialidase using the cell surface optical profilometer (CSOP) (16). The reduction in $\langle h \rangle$ with sialidase treatment is consistent with the deswelling of polyelectrolyte brushes from charge removal. Measurements of RBC surface heights are based on N-terminal labeling of proteins, fluorescein 5-isothiocyanate (FITC)-conjugated *Agaricus bisporus* lectin (ABL) targeting the Gal-GalNac disaccharide, FITC-conjugated *Erythrina cristagalli* lectin (ECL) targeting the Gal-GlcNac disaccharide. (*D*) Average normalized height of multidomain proteins in MD simulations with uncharged (red circles) and charged (cyan and magenta circles) protein residues, where h_0 is the uncharged protein height at dilute densities. Electrostatic interactions among the proteins are modeled by a Yukawa potential with different Debye lengths, κ^{-1}. The simulated decrease in surface protein height upon charge removal is consistent with the CSOP data. For all data, error bars indicate SDs of the mean; N > 3.

poly-LacNac (N-acetyllactosamine) glycans. Given a RBC surface area of 150 μm^2, we estimate a surface density of 6,700/μm^2 for Band 3 ($5 \times 10^5 - 10^6$ copies per cell) and 1,300/μm^2 for GYPA ($1 \times 10^5 - 3 \times 10^5$ per cell) (23, 25).

We found that the K_D of the dextran 40k sensor is ~2.5× larger on the RBC surface compared to that on RBC surfaces treated with broad-spectrum serine protease, proteinase K (ProK) (Fig. 2*B*). We note that ProK treatment leads to only a partial digestion of the cell surface proteins, so the relative crowding state on the untreated wild-type cells are even larger when compared against bare lipid-coated beads (discussed below). To study the role of surface charges, we treated RBCs with sialidase and found that the K_D decreased by 40% compared to the untreated RBC. This result may be surprising given that sialic acids occupy only ~1% of the total cell membrane by mass on RBCs (26). We observed negligible binding of fluorescently labeled *Sambucus nigra* lectin (binds preferentially to sialic acids in α-2,6 linkage) and *Maackia amurensis* lectin II (binds preferentially to sialic acids in α-2,3 linkage) on sialidase-treated RBC surfaces, verifying the proficient removal of sialic acids with sialidase. To verify that negative charge removal is the dominant mechanism of decreased K_D, we used 1-Ethyl-3-(3-dimethylaminopropyl)carbodiimide (EDC) chemistry to neutralize the negative charges on the carboxylic group of sialic acids and other cell surface species (*Materials and Methods*). Consistent with our hypothesis, we found that even a partial neutralization of electrostatic charges reduced K_D to a value comparable to the cells treated with sialidase (Fig. 2*B*). This further confirms that surface crowding cannot be described by surface density nor the protein molecular mass alone, and it demonstrates that surface charge can be a major contributor to crowding.

Because the Debye length is only 0.7 nm in physiological buffers (1), it may be surprising to observe such a strong effect of charge interactions. However, neighboring sialic acids on the O-glycans of GYPA are of the same order as the Debye length based on structural information (27), meaning that intra-chain charge interactions are still relevant. We note that the dextran sensors themselves contain a few charges due to the Alexa Fluor dyes conjugated to the dextran macromolecules, which can change the absolute magnitudes of K_D and K_D^0 individually. However, only the relative difference between the crowded and bare surfaces matters, K_D/K_D^0, so the crowding energy is unaffected as long as the normalized ratio is constant across different sensor chemistries, $\Delta U = k_B T \ln (K_D / K_D^0)$ As a control, we conjugated the dextran macromolecules to a charge-neutral 4,4-Difluoro-4-bora-3a, 4a-diaza-s-indacene (BODIPY) dye, and found that the charges on the dye do not impact the binding kinetics nor crowding energies (*SI Appendix*). Electrostatic interactions between the sensors and the surface sialic acids are likely weak due to the larger separation distances and Debye screening between the dilute sensors and the sialic acids. We also performed control experiments in buffers with pH ranging from 6.0 to 8.0, and we did not observe changes to the binding of our dextran-based sensors, indicating that our results are not a pH-dependent effect from sialic acid removal. Our sensors were also unaffected by lipid-coated beads with 0 to 5 mol % of 1,2-dioleoyl-sn-glycero-3-phospho-L-serine, a lipid that carries a single negative charge on its head group. Lastly, to eliminate the possibility that sialic acid-binding proteins are bound to the cell surface and shield the membrane from sensor binding, we added exogenous sialic acid monosaccharides into the assay buffer to quench the sialic acid-binding proteins; we found no change in our results.

To understand the interplay between charge and glycocalyx architecture, we compared the average thickness of the RBC surface proteins on untreated and sialidase-treated RBCs. We used cell surface optical profilometry (CSOP) (16) to measure glycocalyx thickness by quantifying the height of a fluorophore conjugated to the N-terminus of surface proteins and fluorescent lectins attached to surface glycans (Fig. 2*C*). We found that the average heights of both proteins and glycans reduced by ~30 to 40% with sialidase treatment, consistent with the notion that the polyelectrolyte brushes deswell upon charge removal (22, 28). We tested the effects of charges in-silico by using MD simulations of surface-tethered polyelectrolytes interacting via a screened Coulomb (Yukawa) potential with two different electrostatic interaction distances, 1.0 and 2.0 nm. We found that a surface containing mucin-like glycoproteins swells by ~40% at surface polymer densities of ~15,000/μm^2 (Fig. 2*D*), which is consistent with surface protein densities on cell membranes (21, 29). Our simulations support the hypothesis that the glycocalyx maintains a swollen architecture from electrostatic repulsion, and that the charged glycans pose a significant energy penalty against ligand binding. The mammalian cell surface contains approximately ~10^5 to 10^6 sialic acids/μm^2, (1, 30, 31) which is further elevated in cancers (32, 33), supporting the idea that glycosylation can play an important role in modulating macromolecular binding to the cell surface.

Cell Surface Crowding Is Significant and Varies across Different Cell Types. Motivated by the unique insights obtained from our crowding sensors on human RBCs, we applied them to quantify cell surface crowding of other mammalian cells, including tumor cells with up-regulated glycosylation and sialylation (1). The affinity of our cholesterol-polymer sensors to the cell membrane is in part determined by the chemical affinity of the cholesterol tag with the lipid membrane. Therefore, differences in the native composition of the lipid membrane (particularly cholesterol content) may result in differences in the intrinsic affinity measurement that obscure the surface crowding contribution. While our dextran sensors with adjustable size are useful for comparing different crowding conditions within the same cell type, accurate comparisons between cell types are not possible due to different lipid membrane compositions. To overcome this challenge, we developed a crowding sensor that can measure across different cell types regardless of the cell size, shape, and lipid composition. The sensor consists of two parts—a cholesterol–biotin conjugate that incorporates into the cell membrane from solution (biotin anchor), and a fluorescent anti-biotin IgG antibody (crowding sensor) that measures cell surface crowding based on its binding affinity to the biotin anchor. The biotin anchor also contains a fluorescein 5-isothiocyanate (FITC) fluorophore via thymidine oligonucleotide linker to report its surface density on the membrane (5′-FITC-TTTTTT-biotin-TTT-cholesterol-3′) (Fig. 3*A* and *Materials and Methods*). The IgG size (~12 nm) (34, 35) is similar to our 40k dextran sensor (~10 nm). Control experiments on biotin-containing SLB beads showed a similar ~70% increase in K_D of anti-biotin IgG on a 1% PEG3k brush compared to a bare surface, indicating that our IgG-based sensors are as sensitive to steric crowding as the dextran-40 sensors (*SI Appendix*). Our crowding sensor allows the simultaneous measurement of both the biotin surface density and anti-biotin antibody binding at single-cell resolution (Fig. 3*B*). At a given biotin anchor density, Fig. 3*B* shows that an IgG antibody binds much more readily on a bare bead surface compared to a RBC surface.

The FITC intensity on a cell surface is a readout of the saturating surface concentration of antibody binding, C_{max}, which we use to plot the normalized bound antibody concentration (Fig. 3*C*). Any variations in cell size and surface area become normalized because the bound FITC and antibody intensity is linearly proportional to the cell size (*SI Appendix*). A readout of C_{max} at

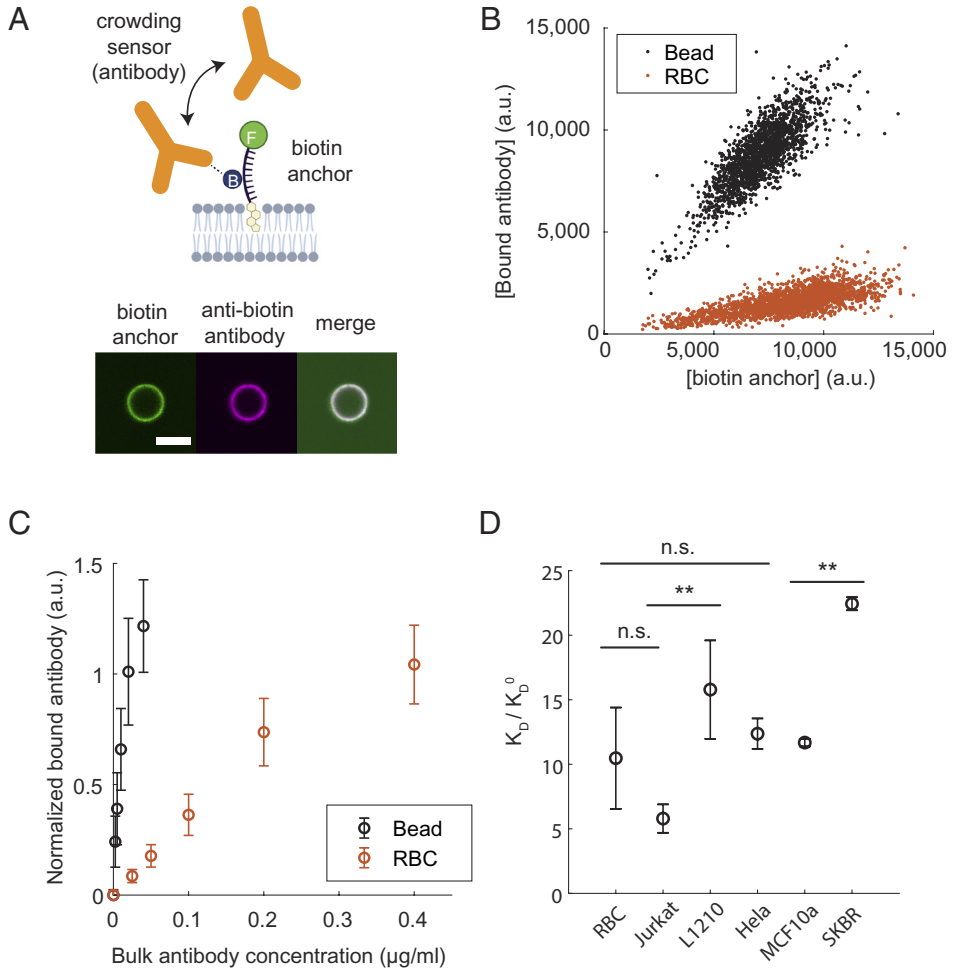

Fig. 3. Cell surface crowding is significant and varies across different cell types. (*A*) Above: Schematic of the two-part crowding sensors that insert into the lipid bilayer with a biotin antigen presented above the membrane. The effective affinity of anti-biotin antibody to the biotin anchor is used as a reporter of surface crowding. Below: Florescence image of a lipid-coated bead with the FITC-biotin-cholesterol construct, anti-biotin antibody, and the merge. (Scale bar is 5 μm.) (*B*) Biotin anchor and the anti-biotin antibody bound on individual RBCs or beads for a fixed bulk antibody concentration, measured with flow cytometry. (*C*) Normalized surface concentration of bound antibody [data from panel (*B*) fitted with a linear slope] as a function of bulk antibody concentration. The ratio of the slopes at small antibody concentrations relative to that of the bare bead is used to determine the normalized dissociation constant on crowded surfaces, K_D/K_D^0. Error bars represent the SD within the same sample. (*D*) Normalized dissociation constant of antibody, K_D/K_D^0, on live suspension and adherent cells. Results are normalized by the binding affinity on bare lipid-coated beads, K_D^0. To prevent internalization of the sensors into the cell interior, cells were incubated on ice throughout the measurement. Error bars represent the SD of the mean in three replicate measurements, except for HeLa and SKBR, which were measured twice. P-values are calculated based on an ANOVA test and Tukey's range test (n.s.: nonsignificant, * < 0.05, ** < 0.01, *** < 0.001).

single-cell resolution enables an accurate measurement of population heterogeneities within a cell sample, which cannot be accomplished using the dextran sensors. The ratio of the slope of the isotherm relative to the slope of the bare bead at small bulk antibody concentrations provides a measurement of K_D/K_D^0. Technically, antibodies have two dissociation constants, K_{D1} and K_{D2}, corresponding to their bivalent binding. In general, the effective dissociation constant depends on a combination of two binding constants, and also the surface antigen concentration (36). Fortunately, at small antigen concentrations (less than ~1,400/μm^2), the effective K_D depends only on a single binding constant and is insensitive to the absolute antigen surface density (*SI Appendix*). At small sensor concentrations, we have verified that our results do not depend on the absolute concentration of the sensors on the surface.

We next compared dissociation constants for different suspension and adherent mammalian cells, normalized by the value on bare beads, K_D^0 (Fig. 3*D*). To prevent internalization of the macromolecules into the cell interior, cells were incubated on ice throughout the measurement. We confirmed using confocal microscopy that the sensors and antibodies are localized on the cell surface and bound homogeneously within the resolution limit (*SI Appendix*). We identified that all mammalian cells tested have surfaces that are significantly more crowded than any reconstituted bead surface evaluated in Fig. 1 (e.g., $K_D/K_D^0 \approx 22$ for SKBR breast epithelial tumor cells compared to $K_D/K_D^0 \leq 2$ on bead surfaces with PEG3k, Fig. 1*E*). This highlights the importance of using native cell membranes to study the physiological impacts of cell surface crowding. As shown in Fig. 3*D*, we observed large variations in crowding across different cell types. For example, SKBR cells displayed 2× more crowding compared to MCF10a cells, which are nonmalignant breast epithelial cells commonly used to model normal breast epithelia behavior. Many mammalian cell surfaces contain a large concentration of sialic acids, which can locally reduce the pH due to its negative charge (1). Because the IgG antibodies are charged macromolecules (unlike our dextran sensors), there may be a pH-dependent binding affinity of IgG onto charged surfaces (37–39). If desired, one could use our neutral dextran sensors within the same cell type to isolate the crowding effects specifically due to charge, as we demonstrated with RBCs.

Cell Surface Crowding Is Altered by Surface Protein Overexpression and Oncogenic Mutations. After observing significant differences in cell surface crowding across different cell types, we asked whether changes in protein expression can alter crowding within a single cell type. To test if our crowding sensor could resolve such changes, we used lentivirus to generate HEK cell lines expressing or overexpressing surface proteins of different heights. Our measurements show that the surface crowding of cells expressing CD43, signal regulatory protein alpha (SIRPα), and E-cadherin increased crowding, while the crowding of Fib1L-expressing cell remains approximately the same (Fig. 4*A*). Interestingly, SIRPα expression increased crowding by approximately 2.5× compared to the wild-type (Fig. 4*B*) and cell–cell crowding variability by ~25% (Fig. 4*C*), whereas CD43 expression increased crowding by less than a factor of 2× (Fig. 4*B*) and cell–cell crowding variability by ~40% compared to the wild

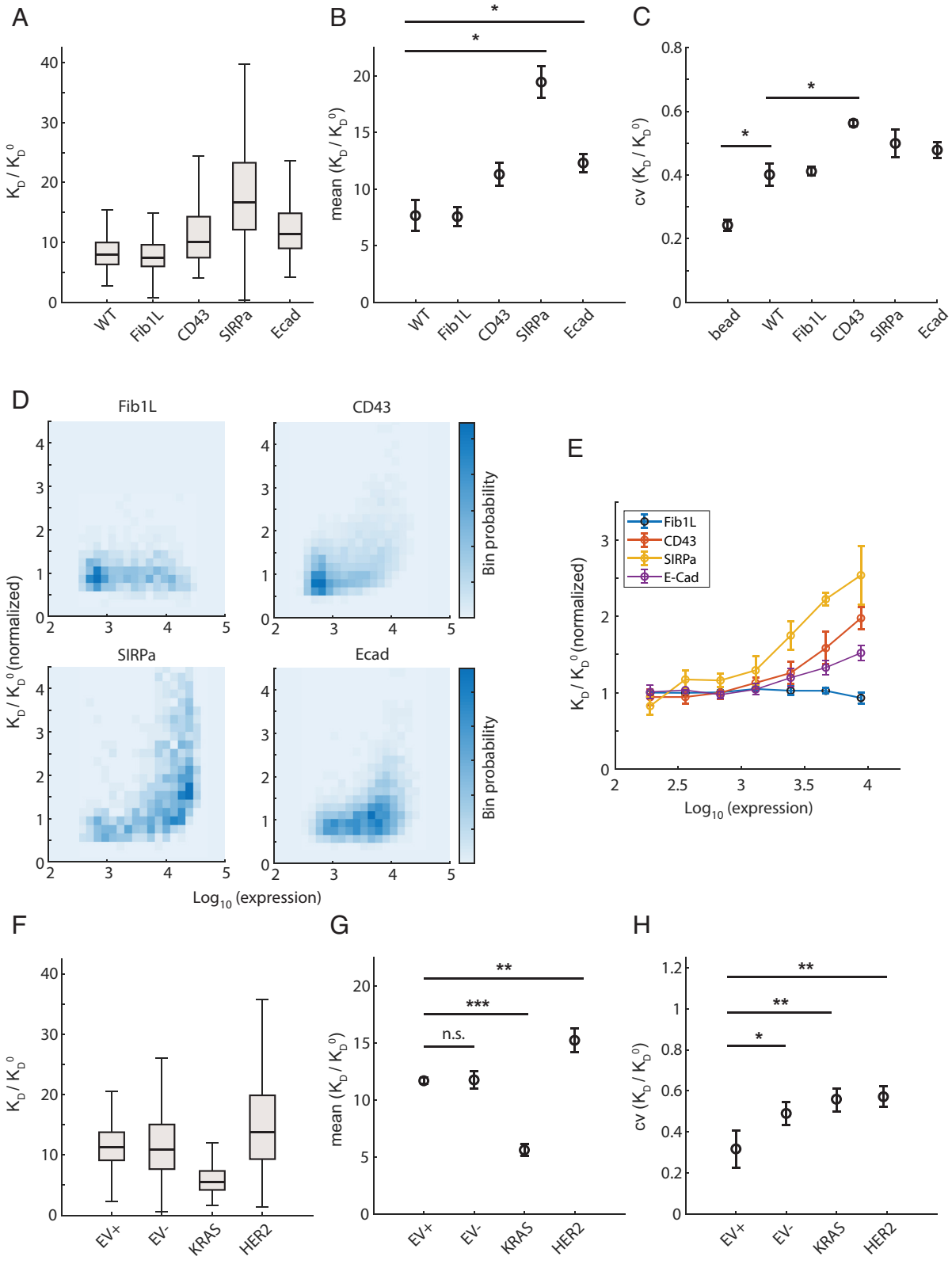

Fig. 4. Mutations and surface protein overexpression alter cell surface crowding and variability. (*A*) Reduction in antibody binding on cells overexpressing various proteins. The distribution is represented as a box and whisker plot showing the median, lower and upper quartiles, and minimum and the maximum values ignoring outliers. To prevent internalization of the sensors into the cell interior, cells were incubated on ice throughout the measurement. N > 300 cells are measured in all conditions in a single run. (*B* and *C*) The mean and coefficient of variance (CV) of affinity change obtained from two replicate measurements. *P*-values are calculated based on an ANOVA test and Tukey's range test (* < 0.05). (*D*) Reduction in antibody-binding affinity as a function of protein overexpression in a bin scatter plot. (*E*) Reduction in antibody-binding affinity as a function of protein overexpression. Error bars represent the SD of the mean from three replicate runs. (*F*) Reduction in antibody-binding affinity in MCF10a and MCF10a transformed with KRAS(G12V) and HER2. The distribution is represented as a box and whisker plot showing the median, lower and upper quartiles, and minimum and the maximum values ignoring outliers. N > 300 cells are measured in all conditions in a single run. EV+: empty vector control supplemented with growth factors. EV-: empty vector control without growth factors. (*G* and *H*) The mean and CV of affinity change obtained from three replicate measurements. *P*-values are calculated based on an ANOVA test and Tukey's range test (* < 0.05, ** < 0.01, *** < 0.001).

type (Fig. 4*C*). We note that the crowding variability measured in the wild type is ~60% larger than that in beads (Fig. 4*C*). This suggests that expression changes within a cell population can lead to both increased mean and variance in crowding. A key advantage of our antibody probe is its ability to measure crowding at single-cell resolution and to obtain a distribution of crowding within a cell population. In the results presented prior to this section, we have focused on the mean surface crowding over an entire cell population. Our results in Fig. 4*C* demonstrate that the variance of the crowding distribution also contains valuable information about the heterogeneities within a cell population.

To further examine the extent of surface crowding observed in different cell lines, we expressed the same surface proteins with a small, 12 residue Spot-tag fused at their N-terminus (16). We measured the crowding sensor binding as a function of protein expression level by quantifying the protein surface density using a fluorescent anti-Spot nanobody (V_{HH}), a small ~2 to 4-nm antibody fragment. We found that crowding increased dramatically as a function of protein overexpression level of CD43, SIRPα, and E-cadherin (Fig. 4*D*). We binned the cells by protein expression level and calculated crowding for each bin, which revealed that SIRPα increases the crowding the most, followed by CD43 and E-cadherin, while for Fib1L, little change was observed over 2 orders of magnitude of expression (Fig. 4*E*). The extracellular domains of Fib 1L, SIRPα, CD43, and E-cadherin, are 89, 317, 204, and 543 amino acids, respectively, underscoring that surface crowding is determined not only by protein molecular mass but by physical properties such as surface charge and structure. Taken together, these results demonstrate that changes in a single protein expression level can significantly alter the total cell surface crowding.

We next tested whether oncogenic transformation alters cell surface crowding using the breast epithelial cell line MCF10a, expressing the common oncogenes HER2 and KRAS(G12V) (40). MCF10a requires growth factors for proliferation but can also maintain homeostasis in the absence of growth factors. We found that MCF10a cells exhibit similar levels of crowding in both proliferating and nonproliferating states (Fig. 4 *F* and *G*). We measured the effect of the oncogenes and found that KRAS-expressing cells decreased crowding by 2× while HER2-expressing cells show slightly increased crowding (Fig. 4*G*). Interestingly, the variance of cell surface crowding was increased in transformed cells when compared to that of EV+, the state of non-malignant growth (Fig. 4 *F* and *H*). Consistent with this, KRAS(G12V) and HER2 expression in MCF10a cells is known to significantly alter the surfaceome as well as glycosylation pattern (41). Furthermore, surface protease activity also changes in KRAS and HER2 cells, cleaving different surface protein groups (42). Our observations suggest that the molecular-level changes in transformed cells result in collective biophysical changes in their cell surface.

Discussion

Traditional biochemical, genetic, and proteomics approaches excel at characterizing the molecular features of membrane proteins (29, 43–46). However, these approaches cannot capture the multibody biophysical interactions on cell surfaces that give rise to crowding. As a result, mechanistic understanding of the biophysical interactions that modulate the organization of the cell surface glycocalyx has been limited. In this work, we developed a simple experimental technique to quantify the impact of cell surface protein glycosylation, density, charge, stiffness, and other physical properties on macromolecular binding to the plasma membrane of live cells.

Our measurements provide a method to quantify the steric energy penalty posed by a crowded cell surface. We found that these energies correspond to ~0.75 to 3 k_BT for the case of IgG binding to buried receptors. These results provide a perspective on what cell surface "crowding" means and how it might be quantified. The free energy posed by the crowded cell surface arises from an osmotic pressure generated by the glycocalyx, given by $\Delta U \approx \Pi V^{\text{eff}}$, where Π is the osmotic pressure and V^{eff} is the effective volume occupied by the macromolecule within the glycocalyx (*SI Appendix*). The free energy may be interpreted as the mechanical work to displace a volume V^{eff} inside a crowded environment with pressure Π. All crowding contributions are captured by the osmotic pressure, including protein glycosylation, density, charge, stiffness, and other physical properties. In *SI Appendix*, we demonstrate using MD simulations that all sensor-binding data collapse onto a universal curve described by a "cell surface equation of state". We propose that the osmotic pressure is a universal metric that acts as a quantitative reporter of cell surface crowding, as opposed to other proxy metrics like protein molecular weight, surface charge, or number density.

Based on our measurements, the cell surface osmotic pressures are given by $\Pi = \Delta U / V^{\text{eff}} = k_B T \ln (K_D/K_D^0)/V^{\text{eff}} = 1-4$ kPa, based on $K_D/K_D^0 \approx 2-20$ and an IgG that excludes a volume based on its size of 10 nm. Note that these absolute pressure values are estimates because an accurate value of the sensors' excluded volume in the glycocalyx is unknown. These approximate values are consistent with the pressures generated by steric crowding interactions between synthetic polymer brushes on membranes, which are sufficient to bend the lipid bilayer (47–49). Interestingly, the surface osmotic pressures measured by our crowding sensors are larger than the stiffness of the cell cytoplasm (~100 Pa), the cell cortex (~1 kPa), and the thick glycocalyx of endothelial cells (100 to 500 Pa), as measured using atomic force microscopy with a large bead tip (50, 51). We anticipate that the 1 to 4 kPa pressures are highly localized just above the membrane surface and that these pressures decay rapidly as a function of distance from the surface into the bulk fluid. Yet, large soluble ligands, antibodies, viruses, and receptors from opposing cell surfaces that bind close to the membrane surface will experience large repulsive pressures. Indeed, we found that the surface crowding can reduce the binding affinity of an IgG antibody to a cell surface by 20×.

We end by noting several areas for future investigation. First, we focused on crowding measurements at a fixed distance very close to the membrane surface. Since the glycocalyx is a fully three-dimensional structure, we anticipate that the surface crowding is height dependent and a measurement of crowding as a function of distance from the membrane may provide further insight into spatial organization. Second, our sensors may be used to study temporal changes in surface protein expression during different stages of the cell cycle, tumor progression, cell senescence, and cell differentiation. Third, while we focused on the extracellular side of the cell membrane, the cytoskeleton on the interior side plays a key role in membrane protein organization, and the interplay between cortical actin organization and glycocalyx crowding mediated by actin-binding proteins merits further study. Fourth, we envision the use of our technique on more complex systems beyond immortalized, individual cells grown on artificial surfaces. If appropriate contrasting agents and reporter tags can be functionalized on our sensors, alternative imaging modalities like ultrasound, X-ray, and MRI may allow a quantification of cell surface crowding in complex

systems, like deep tissues and organoids. Lastly, despite the advances in quantitative transcriptomics and proteomics (29, 43–46), it remains unclear whether and how protein copy number on a cell surface is regulated under physiological conditions or whether surface crowding is simply an unregulated outcome of protein expression, glycosylation, and trafficking. Our crowding sensors may be used to address these and other topics related to the biophysical properties and collective function of the cell surfaceome.

Materials and Methods

Materials. See *SI Appendix* for a listing of materials and resources used for this work.

Protein Purification. Multi-FN3-domain proteins containing C-terminal 10× His-tag and N-terminal ybbR-tags were purified as described previously (20). Briefly, FN3 proteins were expressed in Rosetta DE3 cells (EMD Millipore), lysed by sonication, and purified over a His-Trap HP column (GE Healthcare). The proteins were gel-filtered and their size was confirmed via a Superdex 200 column on an AKTA Pure system (GE Healthcare).

Microscopy. All imaging was carried out on an inverted Nikon Eclipse Ti microscope (Nikon Instruments) equipped with a Yokogawa CSU-X spinning disk using an oil-immersion objective [Apo TIRF 60× and 100×, numerical aperture 1.49, oil]. Three solid state lasers were used for excitation: 488 nm, 561 nm, and 640 nm (ILE-400 multimode fiber with BCU, Andor Technologies). The laser power at the sample plane was less than 1.5 mW for all three channels. Fluorescent light was spectrally filtered with emission filters (535/40 m, 610/75, and 665LP, Chroma Technology) and imaged on a sCMOS camera (Zyla 4.2, Andor Technologies). For CSOP measurements, Z-stack was acquired using a piezo z-stage (nPoint, Inc.).

Synthesis of Crowding Sensors. Cholesterol N-hydroxysuccinimide (NHS) (Nanocs) was dissolved in a 1:2 ratio of ethanol and dimethylsulfoxide (DMSO). Amino 10k dextran and 40k dextran (Invitrogen) and Cholesterol-PEG-amine (Creative PEGWorks, Inc; 966 g/mol MW) were dissolved in DMSO. Equimolar ratio of NHS-dye (choice of AF488, AF555, AF647, or BODIPY), and cholesterol NHS were mixed at a 10:1 molar ratio with cholesterol-PEG-amine, 5:1 molar ratio with 10k dextran amino, 20:1 molar ratio with 40k dextran amino, and left overnight at 50 °C. Control probes without cholesterol conjugation were mixed without cholesterol NHS. To remove unreacted NHS reactants, the reaction mixture was processed through a Zeba Spin Desalting Column, 7K MWCO (Thermo Scientific). The labeling ratio of cholesterol and dye was recorded using a NanoDrop 2000c spectrophotometer (Thermo Scientific).

Small aliquots were stored in −80 °C and used within a few months. Thawed sensors were used within the same day. The labeling ratio of the small sensors is 1 cholesterol/dye, 10k sensor is ~3 cholesterol/dye, and 40k sensor is ~7 cholesterol/dye. The approximate hydrodynamic diameters of the Chol-PEG-dye, dextran 10k, and dextran 40k sensors are ~2, 4, and 10 nm, respectively (19). As a control, we synthesized dextran sensors without the cholesterol anchors and observed no binding to membrane surfaces, verifying that nonspecific interactions between the dextran–dye conjugate and the membrane is negligible (*SI Appendix*).

Preparation of SLB on Glass Beads. Lipid-coated glass beads were created by coating glass microbeads with a fluid SLB. Small unilamellar vesicles (SUVs) were prepared by rehydrating a lipid sheet composed of 1,2-dioleoyl-sn-glycero-3-phosphocholine (DOPC) and other phospholipids with pure deionized water. For SLBs involving the attachment of His-tagged purified proteins, DOPC lipids were mixed with 7.5% of DGS-Ni-NTA. For SLBs involving the binding of anti-biotin antibody, DOPC lipids were mixed with 1% biotinyl cap phosphoethanolamine (PE) and 1% of PEG3k PE. After rehydrating for 30 min, the solution was vigorously vortexed, sonicated at low power (20% power) using a tip-sonicator (Branson Sonifier), and finally filtered through a 0.2-mm filter (Millipore). Stock solutions of SUVs were stored at 4C and were used within 48 h to avoid phospholipid oxidization.

Then, 4.07-μm and 6.46-μm glass micro-bead (Bangs labs) slurry (10% solids) were cleaned using a 3:2 mixture of H_2SO_4:H_2O_2 (Piranha) for 30 min in a bath sonicator, and were spun down at 1,000 g and washed 3 times before being resuspended in pure water. Clean beads were stored in water at room temperature and used within 48 h. To form SLBs, 45 μL SUV solution was added with 5 μL 10× 3-(N-morpholino)propanesulfonic acid (MOPS) buffer (500 mM MOPS pH 7.4, 1 M NaCl) and 10 μL clean bead suspension, and mixed gently. The bead/SUV mixture was incubated for 15 min at room temperature while allowing the beads to sediment to the bottom of the tube. Beads were washed 5 times with 4-(2-Hydroxyethyl)-1-piperazine ethanesulfonic acid (HEPES) buffer (50 mM HEPES pH 7.4, 100mM NaCl) by gently adding/removing the buffer without resuspending the glass beads into solution.

For experiments involving poly His-tagged purified Fibcon and GYPA proteins, 200 nM protein was added into the DGS-Ni-NTA lipid-coated bead solution and incubated at room temperature for 20 min. Beads were washed 3 times with HEPES buffer by gently adding/removing the buffer without resuspending the glass beads into solution. For sialidase-treated GYPA beads, the beads were further treated with 200 mUn/mL sialidase for 30 min at 37 °C. For ProK treated beads, the beads were treated with 0.05 mg/mL ProK for 20 min at 37 °C. Beads were washed 3 times with HEPES buffer. GYPA proteins were fluorescently labeled with NHS-Alexa Fluor 555, and we used confocal microscopy and flow cytometry to verify that the GYPA surface density did not change before and after sialidase treatment.

Preparation of RBCs. Becton Dickinson Microtainer contact-activated lancet was used to withdraw blood from volunteers. A small amount (10 μL) of blood was washed in phosphate-buffered saline (PBS) with 2 mM ethylenediaminetetraacetic acid to remove soluble proteins and plasma from whole blood. RBCs were stored in PBS solution at 4 °C and used within a day. All procedures followed a UC Berkeley IRB approved protocol (CPHS Protocol Number: 2019-08-12454).

To cleave sialic acid from the surface of RBCs, sialidase was used at 50 mUn/mL in PBS at 37 °C for 2 h. No protease activity was found in our stock sialidase (*SI Appendix*). To digest the RBC surface proteins, ProK was added at 0.05 mg/mL in PBS at 37 °C for 1 h. To remove negative charges on carboxylic acid groups on RBC surfaces, 1 mM hydrazide-biotin and 30 mM EDC were mixed with untreated cells in PBS at room temperature for 3 h. The cell surface was visualized with confocal microscopy using fluorescently labeled streptavidin (*SI Appendix*).

RBC measurements were conducted using the synthetic dextran sensors. The small Chol-13xPEG-488 sensor was varied between 0 and 10 nM, the medium 10k-555 sensor was varied between 0 and 15 nM, and the large 40k-647 sensor was varied between 0 and 5 nM.

Flow Cytometry. An Attune NxT Acoustic Focusing Cytometer (ThermoFisher Scientific) was used for all flow cytometry experiments. For RBC measurements, we added ≈10^6 RBC into 1 mL of PBS containing appropriate sensors (typically ≈30 μL stock RBC, containing 10 μL of collected blood in 400 μL of PBS).

Since the crowding energy is given by $\Delta U = k_B T \ln (K_D / K_D^0)$, the important quantity is the ratio of the dissociation constants on a crowded and bare surface, K_D/K_D^0. The absolute magnitudes of K_D for our sensors are unimportant and irrelevant for measuring crowding. We therefore obtain the slope of the bound sensor on a crowded surface at small bulk sensor concentrations, and normalize this value by the slope on bare lipid-coated beads. This provides a direct measurement of the relative difference, K_D/K_D^0, if the bound saturation concentration, C_{max}, is equal on the crowded and bare surfaces: $K_D/K_D^0 = (\theta/C_{bulk})/(\theta^0/C_{bulk}) \approx (C/C_{bulk})/(C^0/C_{bulk})$ if $C_{max} \approx C^0_{max}$. To verify this approach, we performed a control experiment across larger sensor concentration to obtain the full isotherm curve and found similar results for the ratio K_D/K_D^0. In the control experiments, the maximum saturating concentrations of the sensors, C_{max}, were obtained by incubating the beads and RBCs with 0.5 μM bulk sensor concentration. The bound sensor concentrations were normalized by the saturation value to obtain the fractional surface coverage, $\theta = C/C_{max}$. The slope at small bulk concentrations was used to obtain the dissociation constant. A representative dataset containing the full isotherm for the dextran 40k sensor is shown in *SI Appendix*.

For our antibody-based crowding measurements, we first incorporated a FITC-biotin-DNA-cholesterol construct (5′-FITC-TTTTTT-biotin-TTT-cholesterol-3′) into the cell membrane. Therefore, the saturating surface concentration, C_{max}, is set by the total FITC-biotin-DNA-cholesterol inserted into the cell membrane, which we measure directly from the FITC intensity. Because we used small concentrations of the construct in the cell membrane, there was never an excess of unbound antigen at saturating concentrations. As evidence of this statement, we found during our experimental design that the FITC signal reduces to zero when adding a saturating concentration of anti-FITC antibodies in the bulk, which shows that all FITC sites were occupied and quenched due to binding.

Since the synthetic crowding sensors and the monoclonal antibodies are fluorescently labeled, the intensity units from the flow cytometer report the bound sensor concentration. The fractional surface coverage is defined as $\theta = C/C_{max}$, where C is the surface concentration of the sensor on a given sample averaged across ~20,000 events. This fractional surface coverage is plotted as function of bulk concentration of the sensor, and the slope at small bulk sensor concentrations gives the dissociation constant. Since only the ratio K_D/K_D^0 is needed for the crowding energy (as opposed to their individual values), we compare the slopes of the normalized antibody signal from the flow cytometer (antibody channel intensity divided by the FITC channel intensity). We do not need to convert the intensity units into real concentration units because the conversion factor would normalize out when taking the ratio of the slopes. If absolute magnitudes of the individual dissociation constants are needed, fluorescence intensities can be converted to surface concentrations using Quantum Molecules of Soluble Fluorochrome kits (Bangs labs).

We allowed the measurement probes (dextran and biotin antibody) to reach equilibrium on the membrane surfaces for 45 min prior to flow cytometry analysis. A representative time trajectory of sensor binding on RBCs is shown in *SI Appendix*.

In this work, all replicates involving cells indicate biological replicates, in which cells were independently grown and measured on different days.

CSOP Height Measurements on RBCs. PBS solution containing unconjugated wheat germ agglutinin (WGA) was incubated into an 8-well chambered cover glass (Cellvis; catalog number: C8-1.5H-N) to coat the glass with WGA. This helps to immobilize the RBCs when added to the chamber. The chambers were washed and filled with 0.25× PBS in Milli-Q water to swell the RBC into a bloated sphere. Our Chol-13×PEG-488 sensors were added (83 nM) as a membrane reporter. Untreated and sialidase-treated RBCs were added to separate wells. We acquired approximately 15 slices of images straddling the bead equator with a 100-nm step size. Each z-stack image contained up to ten beads per field-of-view. It is critical to locate the equator in both channels to ensure that accurate offsets are calculated (16). More than 100 RBCs were acquired and processed in our custom MATLAB script. Cells with visible defects, including nonspherical shape, membrane tubule and/or bud formation were removed from analysis. In addition, chromatic aberration and other optical offsets were subtracted from our signal by taking a baseline calibration measurement on RBC using our membrane sensor pairs Chol-13xPEG-488 at 83 nM and Chol-13×PEG-647 at 125 nM. The height of the cell surface proteins is obtained by quantifying the difference between the fluorescently labeled height and the aberration offset, $\langle h \rangle = \langle h_{measured} \rangle - \langle h_{offset} \rangle$.

The N-terminal alpha-amines of RBCs were labeled with DyLight 650-4×PEG NHS at 100 μM for 15 min at room temperature in PBS at pH 6.5 (with citric acid). NHS reaction at low pH facilitates preferential labeling of the N terminus (average $pK_a \approx 5-7$) as opposed to other aliphatic amines on the protein (average $pK_a \approx 10.5$) and phosphoethanolamine lipids ($pK_a > 10$) (52). The reaction mixture was washed with PBS to remove excess NHS reagent. Proteinase-K treatment of these cells showed that the majority of the label was removed from the RBC surface, verifying that the NHS reaction predominantly labeled the proteins and not the lipids. For sialidase treatment, the cells were treated with 50 mUn/mL for 1 h at 37 °C to digest sialic acids from the cell surfaces prior to CSOP measurement. No divalent cations (including calcium and magnesium) were added in the measurements, which could result in unwanted cross-linking between negative charges in the glycocalyx.

In addition to N-terminal labeling of RBC surface, we also used lectins as a readout of cell surface height. For height measurements based on lectins, fluorescein labeled *Agaricus bisporus* lectin (ABL), and *Erythrina cristagalli* lectin (ECL) were used. ABL binds to galactosyl (beta-1,3) N-acetylgalactosamine (also called the Thomsen-Friedenreich antigen, or T disaccharide), which are heavily expressed on GYPA proteins on the RBC surface. Unlike peanut agglutinin, which does not bind sialylated T antigen, ABL binds either sialylated or asialylated forms, which makes them good markers for height measurements. Although we noticed a 30 to 50% increase in the binding of ABL to sialidase-treated RBCs, we still observed a strong signal on the fully sialylated surface and assumed that the spatial distribution of bound lectins does not change significantly between untreated and sialidase-treated RBCs. ECL binds to the disaccharide Gal (β1-4) GlcNAc, called LacNAc. Although ECL does not bind to LacNAc terminated with sialic acids, we still observed strong binding on RBCs for all conditions. The single N-glycosylation on the Band3 protein contains LacNAc, which is abundant on the RBC surface. The single complex N-glycan on Band3 is heterogeneous in size, based on the variable repeats of poly-LacNAc units (Gal-β1→4 GlcNAc β 1→3). The end of the oligosaccharide can be linked to sialic acid, fucose, or left exposed.

Coarse-Grained MD Simulations of Protein Polymers and Sensors. To construct a model of macromolecular transport across cell surface proteins and glycocalyx, we performed coarse-grained MD simulations of particle transport within semi-flexible polymers diffusing on two-dimensional surfaces. See *SI Appendix* for a detailed explanation of our simulations. Briefly, we model surface proteins using a Kremer–Grest bead-spring model (53), with each bead representing a structured protein domain or a coarse-grained unit of an intrinsically disordered domain. In this work, the membrane does not deform nor fluctuate in the out-of-plane dimension, although these effects may be included. Simulations were performed using a graphics processing unit-enabled HOOMD-blue MD package (54). A dilute concentration of soluble particles with different sizes were added to model the dynamics of sensor binding to the cell surface. The diameters of the Chol-PEG, 10k, and 40k sensors were modeled with spheres of diameter 3, 5, and 10 nm, respectively.

Mammalian Cell Culture and Preparation.

- HEK293T cells were obtained from University of California, San Francisco (UCSF) Cell Culture Facility and grown in Dulbecco's Modified Eagle Medium (DMEM) (Life Technologies) supplemented with 10% heat-inactivated Fetal Bovine Serum (FBS) (Life Technologies) and 1% Pen-Strep (Life Technologies), at 37 °C, 5% CO2.
- SKBR3 cells were purchased from American Type Culture Collection (ATCC) and grown in McCoy's 5A (ATCC) supplemented with 10% FBS and 1% Pen-Strep.
- Jurkat and L1210 cells were purchased from American Type Culture Collection (ATCC) and is grown in Roswell Park Memorial Institute (RPMI) (Life Technologies) supplemented with 10% FBS, 1% Pen-Strep.
- HeLa cells were obtained from University of California, Berkeley Cell Culture Facility and grown in DMEM (Life Technologies) supplemented with 10% heat-inactivated FBS (Life Technologies) and 1% Pen-Strep (Life Technologies), at 37 °C, 5% CO2.
- MCF10a-derived cell lines expressing oncogenes were a kind gift from Kevin Leung and James Wells at UCSF (41).

For depletion experiments, cells were grown in DMEM supplemented with 5% horse serum, 0.5 mg/mL hydrocortisone, 100 ng/mL cholera toxin, and 1% Pen-Strep. For proliferation experiments, media were further supplemented with 20 ng/mL epidermal growth factor and 10 μg/mL insulin. Cells were passaged by treatment with 0.05% trypsin, and for depletion experiments, by treatment with versene. Cells were passaged every 2 to 3 d. One day prior to flow cytometry experiments, care was taken to seed adherent cells at dilute to intermediate concentrations to prevent the formation of multicell clusters. For suspension cells (RBCs, L1210, Jurkat), cells were washed by centrifuging at 150 g for 1 min and resuspending in PBS to remove media. Adherent cells were carefully scraped from the plastic substrate using a cell scraper and then washed.

To prevent internalization of the sensors into the cell interior, cells were then incubated on ice for 10 to 15 min, and all subsequent steps were performed on ice. 10 to 100 nM of the FITC-biotin-cholesterol sensor was incubated with the cells for 20 min. The final isotherm for the anti-biotin antibody is insensitive to the precise amounts of biotin anchor on the cell surface, as long as the total concentration is low (less than ~1,400/μm^2), as evidenced by the fixed slope of the biotin anchor vs. antibody intensity in the raw flow cytometry data (Fig. 3*B*). Cells were washed thoroughly (5×) in PBS in a centrifuge set to 4C. Finally, the cells were added into tubes prepared with several different Alexa Fluor 647-labeled anti-biotin monoclonal antibody concentration (0 to 0.5 μg/mL). After incubation on ice for 45 min, the samples were measured on the flow cytometer.

Lentiviral Preparation and Cell Line Generation. Lentivirus was produced by transfecting the transfer plasmids, pCMV-dR8.91, and pMD2.G (1.5 μg, 1.33 μg, and 0.167 μg per 35 mm well) into 293T cells grown to approximately 80% confluency using Mirus TransIT-293 Transfection Reagent (Promega) per manufacturer protocol. After 60 to 72 h, supernatant containing viral particles was harvested and filtered with a 0.45-μm filter. Supernatant was immediately used for transduction or aliquoted and stored at −80 °C. Cells were seeded at 20% confluency in 35-mm dishes and 0.5 to 1 mL filtered viral supernatant was added to the cells. Medium containing virus was replaced with fresh growth medium 24 h postinfection. Infected cells were imaged to assess transduction efficiency and then used in flow cytometry assays as described above.

Data, Materials, and Software Availability. All study data are included in the article and/or *SI Appendix*. Raw data files for the main results are available at a publicly accessible database (https://ucsb.box.com/s/1l8bhfbdbtw156kwp2w0drbp1m48oc0s) (55). These data will be accessible upon publication.

ACKNOWLEDGMENTS. We would like to thank Kevin Leung and James Wells at UCSF for a kind gift of MCF10a-derived cell lines. S.C.T. is supported by the Packard Fellowship in Science and Engineering and the NSF (Grant No. 2150686). D.A.F. is supported by NIH R01 GM134137 (D.A.F.), the NSF Center for Cellular Construction (DBI-1548297), and the Miller Institute for Basic Research. D.A.F. is a Chan Zuckerberg Biohub Investigator.

Author affiliations: [a]Department of Bioengineering, University of California, Berkeley, CA 94720; [b]Department of Chemical Engineering, University of California, Santa Barbara, CA 93106; [c]Department of Bio and Brain Engineering, Korea Advanced Institute of Science and Technology, Daejeon, Republic of Korea; [d]University of California, Berkeley/University of California, San Francisco Graduate Group in Bioengineering, Berkeley, CA 94720; [e]Division of Biological Systems and Engineering, Lawrence Berkeley National Laboratory, Berkeley, CA 94720; and [f]Chan Zuckerberg Biohub, San Francisco, CA 94158

1. J.C.-H. Kuo, J. G. Gandhi, R. N. Zia, M. J. Paszek, Physical biology of the cancer cell glycocalyx. *Nat. Phys.* **14**, 658–669 (2018).
2. C. R. Shurer *et al.*, Physical principles of membrane shape regulation by the glycocalyx. *Cell* **177**, 1757–1770.e21 (2019).
3. J.C.-H. Kuo, M. J. Paszek, Glycocalyx curving the membrane: Forces emerging from the cell exterior. *Annu. Rev. Cell Dev. Biol.* **37**, 257–283 (2021).
4. R. A. Kamber *et al.*, Inter-cellular crispr screens reveal regulators of cancer cell phagocytosis. *Nature* **597**, 549–554 (2021).
5. S. B. Biering *et al.*, Genome-wide bidirectional crispr screens identify mucins as host factors modulating sars-cov-2 infection. *Nat. Genet.* **54**, 1078–1089 (2022).
6. D. J. Honigfort, M. H. Zhang, S. Verespy, K. Godula, Engineering of spectator glycocalyx structures to evaluate molecular interactions at crowded cellular boundaries. *Faraday Discuss.* **219**, 138–153 (2019).
7. C. S. Delaveris, E. R. Webster, S. M. Banik, S. G. Boxer, C. R. Bertozzi, Membrane-tethered mucin-like polypeptides sterically inhibit binding and slow fusion kinetics of influenza a virus. *Proc. Natl. Acad. Sci. U.S.A.* **117**, 12643–12650 (2020).
8. C. O. Gurdap, L. Wedemann, T. Sych, E. Sezgin, Influence of the extracellular domain size on the dynamic behavior of membrane proteins. *Biophys. J.* **121**, 3826–3836 (2022).
9. M. Lindén, P. Sens, R. Phillips, Entropic tension in crowded membranes. *PLOS Comput. Biol.* **8**, e1002431 (2012).
10. B. Wollscheid *et al.*, Mass-spectrometric identification and relative quantification of n-linked cell surface glycoproteins. *Nat. Biotechnol.* **27**, 378–386 (2009).
11. H. Du, P. Chandaroy, S. W. Hui, Grafted poly-(ethylene glycol) on lipid surfaces inhibits protein adsorption and cell adhesion. *Biochim. Biophys. Acta* **1326**, 236–248 (1997).
12. S. Rex, M. J. Zuckermann, M. Lafleur, J. R. Silvius, Experimental and monte carlo simulation studies of the thermodynamics of polyethyleneglycol chains grafted to lipid bilayers. *Biophys. J.* **75**, 2900–2914 (1998).
13. H. Jung, *et al.*, Impact of hapten presentation on antibody binding at lipid membrane interfaces. *Biophys. J.* **94**, 3094–3103 (2008).
14. R. Leventis, J. R. Silvius, Quantitative experimental assessment of macromolecular crowding effects at membrane surfaces. *Biophys. J.* **99**, 2125–2133 (2010).
15. J. R. Houser, C. C. Hayden, D. Thirumalai, J. C. Stachowiak, A förster resonance energy transfer-based sensor of steric pressure on membrane surfaces. *J. Am. Chem. Soc.* **142**, 20796–20805 (2020).
16. S. Son *et al.*, Molecular height measurement by cell surface optical profilometry (CSOP). *Proc. Natl. Acad. Sci. U.S.A.* **117**, 14209–14219 (2020).
17. J. M. Noble *et al.*, Direct comparison of optical and electron microscopy methods for structural characterization of extracellular vesicles. *J. Struct. Biol.* **210**, 107474 (2020).
18. A. Halperin, Polymer brushes that resist adsorption of model proteins: Design parameters. *Langmuir* **15**, 2525–2533 (1999).
19. J. K. Armstrong, R. B. Wenby, H. J. Meiselman, T. C. Fisher, The hydrodynamic radii of macromolecules and their effect on red blood cell aggregation. *Biophys. J.* **87**, 4259–4270 (2004).
20. M. H. Bakalar *et al.*, Size-dependent segregation controls macrophage phagocytosis of antibody-opsonized targets. *Cell* **174**, 131–142.e13 (2018).
21. T. Aoki, A comprehensive review of our current understanding of red blood cell (RBC) glycoproteins. *Membranes (Basel)* **7**, 56 (2017).
22. M. Rubinstein, R. H. Colby, *Polymer Physics* (OUP Oxford, 2003).
23. A. H. Bryk, J. R. Wisniewski, Quantitative analysis of human red blood cell proteome. *J. Proteome Res.* **16**, 2752–2761 (2017).
24. A. D. Dupuy, D. M. Engelman, Protein area occupancy at the center of the red blood cell membrane. *Proc. Natl. Acad. Sci. U.S.A.* **105**, 2848 (2008).
25. E.-F. Gautier *et al.*, Absolute proteome quantification of highly purified populations of circulating reticulocytes and mature erythrocytes. *Blood Adv.* **2**, 2646–2657 (2018).
26. S. A. Rosenberg, G. Guidotti, The protein of human erythrocyte membranes: I. Preparation, solubilization, and partial characterization. *J. Biol. Chem.* **243**, 1985–1992 (1968).
27. M. Tomita, H. Furthmayr, V. T. Marchesi, Primary structure of human erythrocyte glycophorin A. Isolation and characterization of peptides and complete amino acid sequence. *Biochemistry* **17**, 4756–4770 (1978).
28. P. J. Flory, *Principles of Polymer Chemistry* (Cornell University Press, 1953).
29. D. Bausch-Fluck *et al.*, The in silico human surfaceome. *Proc. Natl. Acad. Sci. U.S.A* **115**, E10988–E10997 (2018).
30. G. V. Born, W. Palinski, Unusually high concentrations of sialic acids on the surface of vascular endothelia. *Br. J. Exp. Pathol.* **66**, 543–549 (1985).
31. P. M. Kraemer, Sialic acid of mammalian cell lines. *J. Cell. Physiol.* **67**, 23–34 (1966).
32. O. M. T. Pearce, H. Laubli, Sialic acids in cancer biology and immunity. *Glycobiology* **26**, 111–128 (2015).
33. E. Rodrigues, M. S. Macauley, Hypersialylation in cancer: Modulation of inflammation and therapeutic opportunities. *Cancers* **10**, 207 (2018).
34. C. De Michele, P. De Los Rios, G. Foffi, F. Piazza, Simulation and theory of antibody binding to crowded antigen-covered surfaces. *PLOS Comput. Biol.* **12**, e1004752 (2016).
35. Y. H. Tan *et al.*, A nanoengineering approach for investigation and regulation of protein immobilization. *ACS Nano* **2**, 2374–2384 (2008).
36. T. Yang, O. K. Baryshnikova, H. Mao, M. A. Holden, P. S. Cremer, Investigations of bivalent antibody binding on fluid-supported phospholipid membranes: The effect of hapten density. *J. Am. Chem. Soc.* **125**, 4779–4784 (2003).
37. G. Ruiz, K. Tripathi, S. Okyem, J. D. Driskell, pH impacts the orientation of antibody adsorbed onto gold nanoparticles. *Bioconjugate Chem.* **30**, 1182–1191 (2019).
38. T. Sulea *et al.*, Structure-based engineering of ph-dependent antibody binding for selective targeting of solid-tumor microenvironment. *MAbs* **12**, 1682866 (2020).
39. H. Jung, A. D. Robison, P. S. Cremer, Detecting protein–ligand binding on supported bilayers by local pH modulation. *J. Am. Chem. Soc.* **131**, 1006–1014 (2009).
40. M. M. Martins *et al.*, Linking tumor mutations to drug responses via a quantitative chemical–genetic interaction map. *Cancer Discovery* **5**, 154–167 (2015).
41. K. K. Leung *et al.*, Broad and thematic remodeling of the surfaceome and glycoproteome on isogenic cells transformed with driving proliferative oncogenes. *Proc. Natl. Acad. Sci. U.S.A.* **117**, 7764–7775 (2020).
42. K. Schaefer *et al.*, Direct identification of proteolytic cleavages on living cells using a glycan-tethered peptide ligase. *ACS Central Sci.* **8**, 1447–1456 (2022).
43. D. Bausch-Fluck *et al.*, A mass spectrometric-derived cell surface protein atlas. *PLoS One* **10**, e0121314 (2015).
44. C. Klijn *et al.*, comprehensive transcriptional portrait of human cancer cell lines. *Nat. Biotechnol.* **33**, 306–312 (2015).
45. S. B. Pollock *et al.*, Highly multiplexed and quantitative cell-surface protein profiling using genetically barcoded antibodies. *Proc. Natl. Acad. Sci. U.S.A* **115**, 2836 (2018).
46. M. Stoeckius *et al.*, Simultaneous epitope and transcriptome measurement in single cells. *Nat. Methods* **14**, 865–868 (2017).
47. D. J. Busch *et al.*, Intrinsically disordered proteins drive membrane curvature. *Nat. Commun.* **6**, 7875 (2015).
48. P. L. Hansen, J. A. Cohen, R. Podgornik, V. A. Parsegian, Osmotic properties of poly(ethylene glycols): Quantitative features of brush and bulk scaling laws. *Biophys. J.* **84**, 350–355 (2003).
49. A. K. Kenworthy, K. Hristova, D. Needham, T. J. McIntosh, Range and magnitude of the steric pressure between bilayers containing phospholipids with covalently attached poly (ethylene glycol). *Biophys. J.* **68**, 1921–1936 (1995).
50. R. O'Callaghan, K. M. Job, R. O. Dull, V. Hlady, Stiffness and heterogeneity of the pulmonary endothelial glycocalyx measured by atomic force microscopy. *Am. J. Physiol. Lung Cell. Mol. Physiol.* **301**, L353–L360 (2011).
51. J. Rheinlaender *et al.*, Cortical cell stiffness is independent of substrate mechanics. *Nat. Mater.* **19**, 1019–1025 (2020).
52. C. B. Rosen, M. B. Francis, Targeting the n terminus for site-selective protein modification. *Nat. Chem. Biol.* **13**, 697 (2017).
53. K. Kremer, G. S. Grest, Molecular dynamics (MD) simulations for polymers. *J. Phys. Condens. Matter* **2**, SA295–SA298 (1990).
54. J. A. Anderson, J. Glaser, S. C. Glotzer, Hoomd-blue: A python package for high-performance molecular dynamics and hard particle monte carlo simulations. *Comput. Mater. Sci.* **173**, 109363 (2020).
55. S. C. Takatori *et al.*, Data file for "Engineered molecular sensors for quantifying cell surface crowding". Box. https://ucsb.box.com/s/1l8bhfbdbtw156kwp2w0drbp1m48oc0s. Accessed 2 May 2023.

Supporting Information

Engineered molecular sensors for quantifying cell surface crowding

Authors: Sho C. Takatori[a,e,1,2], Sungmin Son[a,f,1,2], Daniel S.W. Lee[a], and Daniel A. Fletcher[a,b,c,d,2]

[a] Department of Bioengineering, University of California, Berkeley, Berkeley, CA 94720, USA
[b] UC Berkeley/UC San Francisco Graduate Group in Bioengineering, Berkeley, CA 94720, USA
[c] Division of Biological Systems and Engineering, Lawrence Berkeley National Laboratory, Berkeley, CA 94720, USA;
[d] Chan Zuckerberg Biohub, San Francisco, CA 94158, USA
[e] Department of Chemical Engineering, University of California, Santa Barbara, Santa Barbara, CA 93106, USA.
[f] Department of Bio and Brain Engineering, KAIST, Daejeon, Republic of Korea.

[1] S.C.T. and S.S. contributed equally to this work.

[2] To whom correspondence should be addressed. E-mail: stakatori@ucsb.edu ; smson@kaist.ac.kr ; fletch@berkeley.edu

Chapter I. Dynamics of macromolecular binding on crowded surfaces

The goal of this chapter is to develop a theory of macromolecular adsorption to identify a quantitative metric of surface crowding. We aim to obtain a direct relationship between surface binding of soluble macromolecules and the crowding state of the surface, including the effects of variable glycoprotein length, polydispersity, stiffness, density, charge, and all other interactions. We propose that the osmotic pressure is a universal metric that acts as a quantitative reporter of cell surface crowding, as opposed to other proxy metrics like protein molecular weight or number density.

1. Momentum balance on crowded cell membrane surfaces

The Cauchy momentum balance in a control volume above the cell surface is given by

$$\rho \frac{D\boldsymbol{u}}{Dt} + \nabla \cdot \boldsymbol{\sigma} + \boldsymbol{b} = \boldsymbol{0}, \tag{1.1}$$

where *D/Dt* is a material derivative, $\boldsymbol{u}$ is the suspension average velocity, $\boldsymbol{\sigma}$ is the total stress of the suspension, and $\boldsymbol{b}$ is an external force. Incompressibility further requires that $\nabla \cdot \boldsymbol{u} = 0$. The total suspension stress, which include both the fluid and the surface polymers, is given by

$$\boldsymbol{\sigma} = -p_f \boldsymbol{I} + 2\eta_0(1 + 5\phi/2)\boldsymbol{E} + \boldsymbol{\sigma}^{(P)}, \tag{1.2}$$

where p_f is the fluid pressure, η_0 is the viscosity of the continuous Newtonian solvent, $\boldsymbol{E}$ is the rate-of-strain tensor, ϕ is the volume fraction of particles (= $4\pi a^3 n/3$ for spheres), n is the number density, $5\phi/2$ is the Einstein shear viscosity correction that is present for all suspensions, and the particle contribution to the stress $\boldsymbol{\sigma}^{(P)} = -nk_BT\,\boldsymbol{I} + \boldsymbol{\sigma}^P$, where $\boldsymbol{\sigma}^P = -n\langle \boldsymbol{x}_{ij}\boldsymbol{F}_{ij}\rangle$ is the virial stress contribution from interparticle interactions. The force $\boldsymbol{F}_{ij}$ includes all interparticle interactions between the particles.

At low Reynolds numbers and in the absence of external forces, the momentum balance of the suspension (solvent plus any particles and polymers) at equilibrium is

$$\nabla \cdot \boldsymbol{\sigma} = \boldsymbol{0}. \tag{1.3}$$

It is important to note that an aqueous polymer brush surface is at minimum a 2-component system: the fluid plus the particles (polymers). Therefore, the total suspension stress includes contributions from both the solvent and the particles (polymers), $\boldsymbol{\sigma} = -p_f \boldsymbol{I} + \boldsymbol{\sigma}^{(P)}$. Therefore, at every continuum point in the suspension, the overall pressure is a sum of the local fluid pressure, p_f, and the osmotic pressure from interactions among the particles within the suspension, including polymers, free ions, and other interacting particles, $\Pi = -\mathrm{tr}\,\boldsymbol{\sigma}^{(P)}/3$ (see Fig. S1.1). If there are free ions in solution, then those electrolytes would generate an additional osmotic pressure that is included within Π via the stresslet $\langle \boldsymbol{x}_{ij}\boldsymbol{F}_{ij}\rangle$. Assuming that there are no fluid velocities and that the system is translationally invariant (i.e., independent of in-plane coordinates *x* and *y*), Eq. (1.3) becomes $\partial\sigma_{zz}/\partial z = 0$. This reveals that the total suspension stress is constant everywhere along the z-direction (normal to the membrane surface).

Using Fig. S1.1, we shall conduct a momentum balance to clarify the relationship between the osmotic pressure and swelling of the polymer brush. Suppose that we perform a macroscopic momentum balance on the two regions indicated: bulk solution far away from the brush, and at a point within the brush. At equilibrium, the fluid pressure in the bulk and inside the brush must be equal; otherwise, we would get net flux of solvent to rush from one side to the other. Therefore, $p_f^{\mathrm{bulk}} = p_f^{\mathrm{brush}}$. Since the region inside the polymer brush also contains interactions among the polymer beads, these interactions generate an osmotic pressure, Π. This osmotic pressure increases the chemical potential of the solvent in the solution so that it equals that of the excess solvent surrounding the swollen polymer brush. The elastic swelling reaction of the network structure may be interpreted as a pressure acting on the solution, or swollen gel. The chain

stretching and network swelling exactly balances the osmotic pressure generated by their interactions, in such a way that the overall momentum balance is satisfied. Therefore, polymer brush swelling and osmotic pressures are equivalent descriptions of the equilibrium structure of the polymer brush. Once we have a constitutive relation for the polymer, we can directly equate the osmotic pressure with the network swelling to determine the shape and size of the polymer gel. For example, the swelling of a gel is given by Eq. (3.75) in Doi (Soft Matter Physics, 2013) (1):

$$\Pi = G_0 \left(\frac{\phi}{\phi_0}\right)^{1/3}, \tag{1.4}$$

where ϕ is the volume fraction of polymers in the gel (i.e., metric of gel swelling), ϕ_0 is the volume fraction in the reference state, and G_0 is the shear modulus of the gel in the reference state. Paraphrasing Doi's text, the left hand side of Eq. (1.4) represents the force that drives polymers to expand and mix with the solvent, while the right-hand side represents the elastic restoring force of the polymer network which resists expansion. The equilibrium volume of the gel is determined by the balance of these two forces. Once again, this demonstrates that the polymer brush height and osmotic pressures are equivalent descriptions of the equilibrium structure of the polymer brush.

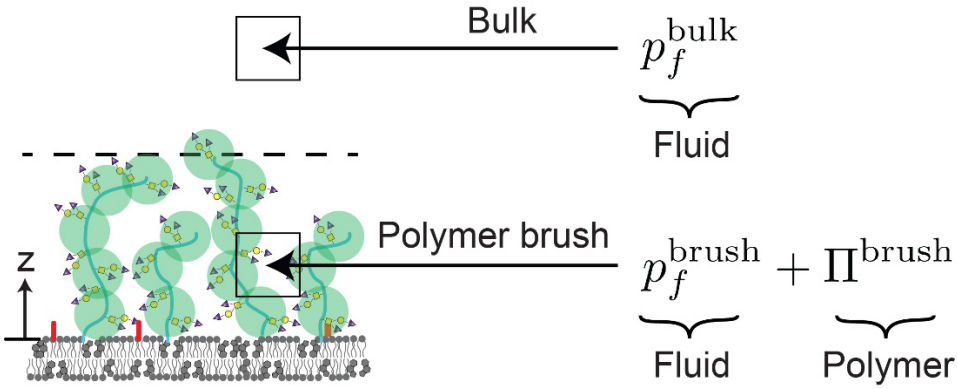

Figure S1.1: Cartoon illustrating the overall suspension pressure, which is composed of both a fluid pressure and the particle (polymer) osmotic pressure. Network swelling and osmotic pressures are equivalent descriptions of the equilibrium structure of the polymer brush.

In the x- and y-directions (tangent to membrane surface), the particle stress can take on any value, $\sigma_{xx}^{(P)} \neq 0$ and $\sigma_{yy}^{(P)} \neq 0$. We therefore have an anisotropic particle stress tensor, $\boldsymbol{\sigma}^{(P)} = \sigma_{xx}^{(P)} \boldsymbol{e}_x \boldsymbol{e}_x + \sigma_{yy}^{(P)} \boldsymbol{e}_y \boldsymbol{e}_y + \sigma_{zz}^{(P)} \boldsymbol{e}_z \boldsymbol{e}_z$, with $\sigma_{zz}^{(P)} = 0$. The mechanical (osmotic) pressure is defined as $\Pi = -\text{tr}\,\boldsymbol{\sigma}/3$, and we define the in-plane pressure of cell surfaces as

$$\Pi = -\left(\sigma_{xx}^{(P)} + \sigma_{yy}^{(P)}\right)/2\,. \tag{1.5}$$

This is the in-plane pressure that we report in this document for both experiments and simulations.

2. Equation of state (EOS) of crowded membrane surfaces

Modeling the cell surface proteins and glycans as coarse-grained polymers, we can obtain an equation of state relating the osmotic pressure of the cell surface suspension as a function of its material properties, including density, contour length, persistence length, and electrostatic charge.

The equation of state for hard-sphere colloidal suspensions, including the Carnahan-Starling EOS, is used commonly to model macromolecular crowding on the membrane surface and inside the cytoplasm (2-

5). Here, we use our data from molecular dynamics (MD) simulations to determine the equation of state for cell surfaces (see Chap. II for details of MD simulations). The EOS may be represented as a virial expansion (6):

$$\Pi = \frac{k_B T}{V_p}\left(\frac{\phi}{N_R} + B_2\phi^2 + B_3\phi^3 + \cdots\right), \tag{1.6}$$

where $V_p = \pi\sigma^3/6$ is the volume of a monomer, $N_R = L/\sigma$ is the degree of polymerization, B_2 and B_3 are the second and third virial coefficients and describe two-body and three-body interactions, respectively. For Weeks-Chandler-Andersen (WCA) potentials between all particles, $B_2 > 0$ and $B_3 > 0$, and the pressure increases beyond the ideal-gas value.

As shown in Fig. S1.2, we find that truncation at the three-body level gives a proficient agreement over the concentrations that we tested in MD. For charge-neutral polymer surfaces, $B_2 = 0.40$, $B_3 = 7.93$. For charged polymers with Debye length $\kappa^{-1} = 1\sigma$, we obtain $B_2 = 2.22$, $B_3 = 10.81$; for $\kappa^{-1} = 2\sigma$, we obtain $B_2 = 2.68$, $B_3 = 29.67$.

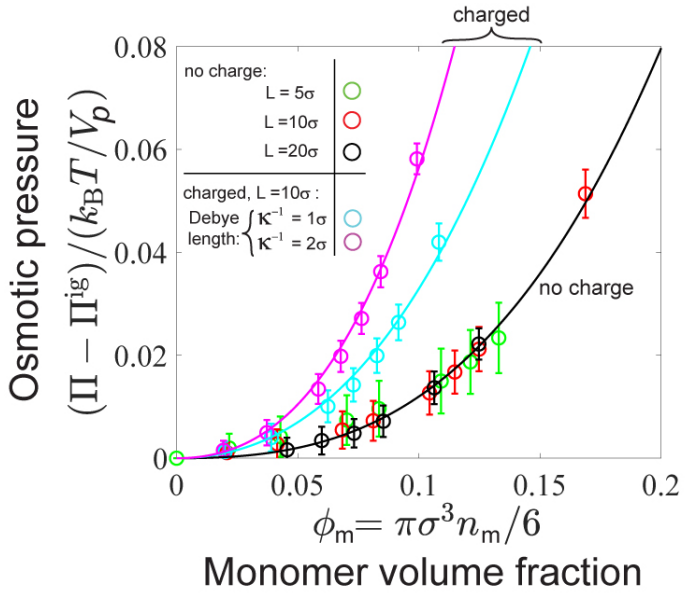

Figure S1.2: Coarse-grained molecular dynamics (MD) simulations were used to compute the osmotic pressure generated by polymers tethered to a membrane surface. The osmotic pressure is defined by Eqs. 1.5 and 1.6, and the ideal-gas pressure has been subtracted in this plot, $\Pi^{ig} = k_B T\phi/(V_p N_R)$, where V_p is the volume of a monomer and $N_R = L/\sigma$ is the degree of polymerization. The symbols are simulation data, and the solid curves are Eq. 1.6.

3. Analytical theory for brush inclusion penalty

Halerpin et al. (7-9) have conducted theoretical analyses of soluble protein adsorption onto chemically grafted polymer brush surfaces. They distinguish between an insertion versus compressive mechanism of protein adsorption, depending on the size of the protein compared to the mesh size of the polymer brush. One key difference between chemically grafted polymer brushes and the cell surface glycoprotein brush is that a significant fraction of transmembrane proteins is mobile and can translate in 2D along the lipid bilayer surface. Therefore, a large macromolecule may adsorb onto the membrane via the insertion mechanism because it is energetically more favorable to exclude polymers from the interface as opposed to compressing the brush.

To obtain the free energy of inserting a large macromolecule into the cell surface glycocalyx, we follow the theory by Louis et al (10). The inclusion energy of a colloid in a polymer suspension is given by

$$\Delta U = \Pi(\phi)V_s + \gamma(\phi)A_s, \tag{1.7}$$

where $\Pi(\phi)$ is the osmotic pressure, $\gamma(\phi)$ is the interfacial tension, V_s is the volume of the macromolecule ($= 4\pi R^3/3$ for spheres), and A_s is the surface area of the macromolecule ($= 4\pi R^2$ for spheres). The first term in Eq. 1.7 is the reversible work required to create a cavity of volume V_s within the polymer brush. The second term is the energy penalty associated with creation of a depletion layer around the colloid surface. The osmotic pressure term has been discussed earlier and is given by Eq. 1.6.

The interfacial tension for a planar interface is given by

$$\gamma(\phi) = -\Pi(\phi)\Gamma(\phi) + \int_0^{\phi} \Pi(\phi') \left(\frac{\partial \Gamma(\phi')}{\partial \phi'}\right) d\phi', \tag{1.8}$$

where the relative adsorption $\Gamma(\phi)$ captures the effect of changes in local polymer density due to the creation of an interface. The adsorption is defined as

$$\Gamma(\phi) = \int_0^{\infty} \left(\frac{\phi(r)}{\phi(r \to \infty)} - 1\right) dr, \tag{1.9}$$

where r is the distance from the colloid surface. The leading order expression of the adsorption is approximated by $\Gamma \approx -2R_g/\sqrt{\pi} \approx -R_g$. This assumes that the adsorption is independent of local density and behaves as an ideal polymer. With this approximation, the surface tension is described solely by the entropic free energy penalty of creating an additional cavity of volume $\Gamma A_s \approx R_g A_s$, in addition to the volume of the sensor V_s.

Using this approximation, the surface tension term can be incorporated into a bulk osmotic pressure term in the insertion free energy as

$$\Delta U \approx \Pi(\phi)V^{\text{eff}}, \tag{1.10}$$

where the effective volume of the cavity due to macromolecular insertion is $V^{\text{eff}} = 4\pi R^3/3 + 4\pi R^2 R_g$ for a spherical polymer blob of size R_g and macromolecule of size R (see Fig. S1.3). For our system with $R \approx R_g$, the effective volume is well-approximated as $V^{\text{eff}} = 4\pi(R + R_g)^3/3$.

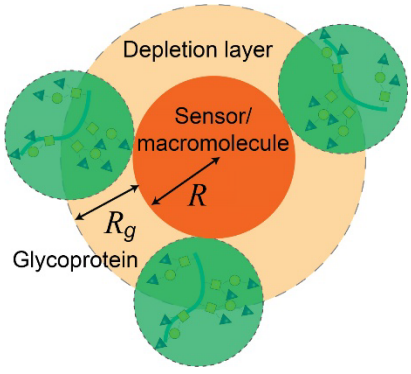

Figure S1.3: Schematic of the depletion layer and cavity related to the inclusion free energy of a colloid inside a polymer brush suspension. The size R is the radius of the macromolecule and R_g is the radius of gyration of the glycoprotein.

We use coarse-grained MD simulations to validate our theory. As shown in Fig. S1.4(A), when the insertion energy is plotted as a function of the surface density of polymers, there is no collapse of the data across different sensor sizes and lengths of the polymer brush. This indicates that the surface density is not an accurate, quantitative metric of crowding. Other proxy metrics like molecular weight and number density are inadequate to characterize crowding, because they do not include effects of variable glycoprotein length, polydispersity, stiffness, density, charge, and other interactions.

However, when the energy is plotted as a function of the osmotic pressure, the data collapse onto a master curve, as shown in Fig. S1.4(B). It is important to note that there is no adjustable fitting parameters here. These results confirm our hypothesis that the surface osmotic pressure is the unique quantity that provides a direct, quantitative metric of crowding. When quantifying crowding effects on cell surfaces, one should use the osmotic pressure instead of other proxy metrics like molecular weight, size, and surface density of the surface proteins.

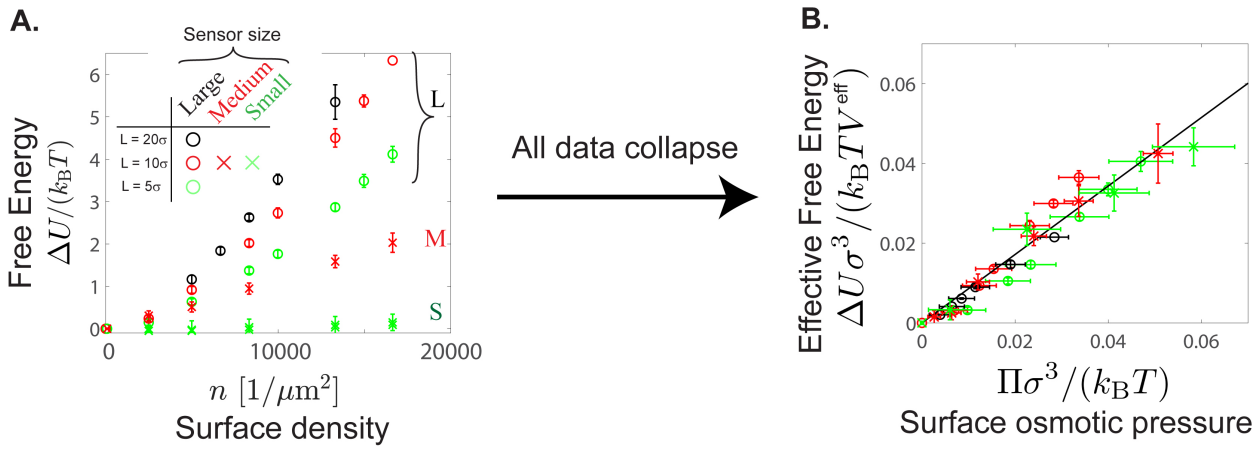

Figure S1.4: Insertion energy for large ($R = 2\sigma$), medium ($R = \sigma$), and small ($R = \sigma/2$) sensors as a function of surface polymer number density and contour lengths. (A) Insertion energy for the sensors as a function of surface density of polymers. The data do not collapse onto a universal curve, indicating that the surface density is not an accurate metric of surface crowding. (B) Normalized insertion energy, $\Delta U\sigma/(k_BTV^{\text{eff}})$, where $V^{\text{eff}} = 4\pi(R + R_g)^3/3$ is the excluded volume of the sensor in the polymer brush. Data across different sensor sizes and surface polymer contour lengths collapse onto a universal line when plotted as a function of osmotic pressure Π.

4. Analytical theory for effective brush potential

In our coarse-grained MD simulations, the Weeks-Chandler-Andersen (WCA) repulsive potential (11) was implemented between the polymer-polymer, polymer-sensor, polymer-substrate, and sensor-substrate. For the sensor-substrate interactions, we also add an attractive Morse potential to model affinity of the sensor to the membrane, which effectively approximates a short-range, attractive harmonic potential, $k(z-r_0)^2/2$, with stiffness k. These two potentials are sufficient to predict the free-energy landscape for the bare membrane simulations.

$$U_0 = \begin{cases} U_{\text{WCA}} + U_{\text{att}} & \text{if } z < 2^{1/6}R \quad (1.11) \\ U_{\text{att}} & \text{if } 2^{1/6}R < z < (2^{1/6}R + R) \quad (1.12) \\ 0 & \text{if } z > (2^{1/6}R + R) \quad (1.13) \end{cases}$$

where the repulsive WCA potential is given by

$$U_{\mathrm{WCA}} = 4\epsilon\left[\left(\frac{R}{z}\right)^{12} - \left(\frac{R}{z}\right)^{6}\right] + \epsilon \tag{1.14}$$

and the attractive potential to the membrane surface is given by

$$U_{\mathrm{att}} = k(z-R)^2/2\ . \tag{1.15}$$

Obtaining the ΔU contribution to the overall free energy is non-trivial, since we only include WCA potentials for sensor-polymer interactions and no explicit potential of the brush into the sensor's equation of motion. We do not apriori know what the effective potential posed by the polymer brush will be.

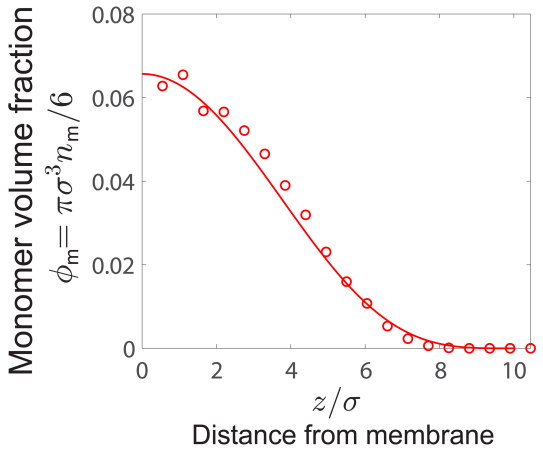

Figure S1.5: Local monomer volume fraction as a function of distance from the membrane, for a surface density of 8000 chains/μm^2. The symbols are simulation data, and the solid curve is Eq. 1.16.

From MD simulation data, the monomer volume fraction of the polymers as a function of height from the membrane surface is modeled by

$$\phi_m = \phi_m^0\left[1 - \left(\frac{z}{L}\right)^2\right]^4. \tag{1.16}$$

We verified that this model for the polymer brush agrees with data from MD simulations, as shown in Fig. S1.5. The parabolic form inside the brackets is well known from polymer theory (12); we observe a steeper decay of density, likely due to the fact that the chains are not grafted and instead free to diffuse in 2D. The free energy of a sensor binding to a crowded polymer surface is given by

$$U = \begin{cases} U_{\mathrm{WCA}} + U_{\mathrm{att}} + \Delta U & \text{if } z < 2^{1/6}R \quad (1.17) \\ U_{\mathrm{att}} + \Delta U & \text{if } 2^{1/6}R < z < (2^{1/6}R + R) \quad (1.18) \\ \Delta U & \text{if } z > (2^{1/6}R + R) \quad (1.19) \\ 0 & \text{if } z > L \quad (1.20) \end{cases}$$

Substituting Eq. 1.16 into the virial pressure equation of state, Eq. 1.6, gives the local osmotic pressure as a function of distance from the membrane surface. The crowding energy as a function of distance, $\Delta U(z)$, is obtained by using Eq. 1.10. The resulting crowding energy is used in Eqs. 1.17 – 1.20 to obtain the total energy as a function of distance, $U(z)$. As shown in Fig. S1.6, the data from our MD simulations (black symbols) demonstrate excellent agreement with our theory (red curve).

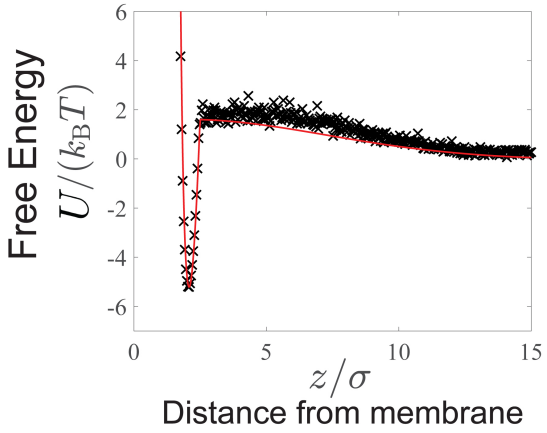

Figure S1.6: Full free energy curve using Eqs. 1.17 - 1.20 (solid red curve) agrees with the direct calculation from the sensor probability distribution (black crosses). There are no adjustable parameters in the theoretical model, Eqs. 1.17 – 1.20.

Chapter II. Coarse-grained molecular dynamics (MD) simulations

1. Basic construction of the model

To construct a molecular model of macromolecular transport across cell surface proteins and glycocalyx, we performed coarse-grained Molecular Dynamics (MD) simulations of colloidal transport within semi-flexible polymers diffusing on 2D surfaces. This is a modified extension of our protein polymer surface model presented previously (13).

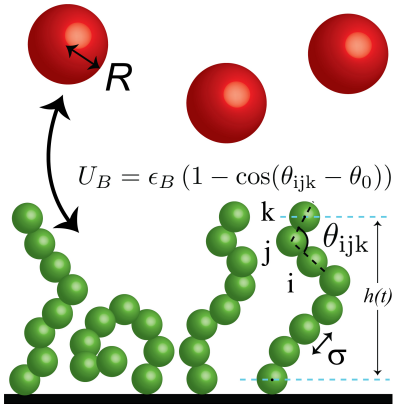

Figure S2.1: Schematic of our coarse-grained MD simulations of a protein polymer brush with surface-binding macromolecular sensors. Using a Kremer-Grest bead-spring model (14), individual beads of diameter σ are connected by a finitely extensible nonlinear elastic (FENE) potential and a bending stiffness is invoked by a 3-particle angular potential, U_B. The bottom bead is confined to remain along a 2D surface but can diffuse laterally along the surface. Sensor particles of size R are added to the bulk above the polymer brush. The sensors have a short-ranged binding affinity to the substrate.

We modeled surface protein chains using a Kremer-Grest bead-spring model (14), with each bead representing a structured protein domain or a coarse-grained unit of an intrinsically disordered domain. A bead at one end of the chain is confined between two parallel walls separated by one bead diameter, allowing it to diffuse freely in 2D but cannot escape out of plane. All other beads on the chain are free to move in

3D, except through a bottom wall that acts as a solid substrate, thereby modeling protein diffusion along a membrane that is in-plane fluid. Because the size of each protein domain is large compared to the surrounding solvent molecules, the solvent is coarse grained and its dynamics are not explicitly evolved. In other words, the protein chain experiences a hydrodynamic drag and Brownian motion from the continuous solvent. In this work, the membrane does not deform nor fluctuate out of plane, although these effects may be included.

Simulations were performed using a GPU-enabled HOOMD-blue molecular dynamics package (15,16), and all simulations contained at least 2000 protein chains and 10000 sensor particles. The dynamics of particle i is evolved in time following the overdamped Langevin equation

$$\mathbf{0} = -\zeta_i \boldsymbol{U}_i + \boldsymbol{F}_i^B + \boldsymbol{F}_i^P, \tag{2.1}$$

where ζ_i is the hydrodynamic drag factor, $\boldsymbol{U}_i$ is the velocity, $\boldsymbol{F}_i^B = \sqrt{2\zeta_i^2 D_i}\boldsymbol{\Lambda}$ is the translational Brownian force, D_i is the Stokes-Einstein-Sutherland translational diffusivity of a single monomer, and $\boldsymbol{F}_i^P$ is the interparticle force. The left-hand side is zero since inertia is negligible for coarse-grained proteins embedded in a viscous solvent. The translational diffusivity is modeled with the usual white noise statistics, $\langle \boldsymbol{\Lambda}(t) \rangle = \mathbf{0}$ and $\langle \boldsymbol{\Lambda}(t)\boldsymbol{\Lambda}(0) \rangle = \delta(t)\, \boldsymbol{I}$, where $\delta(t)$ is a delta function and $\boldsymbol{I}$ is the identity tensor. The drag coefficient ζ_i of particle i is linearly scaled with the particle size σ_i. The interparticle force (described below) includes contributions from sensor-polymer chain interactions, intrachain polymer potential, interchain bead-bead pair interactions, and bead-wall interactions.

All interactions between the particles and walls are modeled with a Weeks-Chandler-Andersen (WCA) potential (11), in which a Lennard-Jones (LJ) potential is shifted upwards, truncated at the potential minimum of $2^{1/6}\,\sigma_i$ (such that the potential is purely repulsive), and assigned a well depth of $\epsilon = k_B T$ (where $k_B T$ is the thermal energy). All lengths are expressed in units of the LJ diameter σ and is set to unity. We connect the polymer chains with a finitely extensible nonlinear elastic (FENE) potential, using a spring constant of $k_0 = 30$ and a bond length of $R_0 = 1.5$ (expressed in terms of reduced LJ units, $\epsilon = \sigma = 1$). To model semi-flexible polymers, we implemented a bending potential between 3 neighboring particles to capture chain stiffness, $U_B = \epsilon_B\big(1 - \cos(\theta_{\mathrm{ijk}} - \theta_0)\big)$, where U_B is the bending energy, θ_{ijk} is the bond angle between neighboring particles (i,j,k), and $\theta_0 = \pi$ is the resting angle. The persistence length of the chains was measured by calculating the bond angle correlation, $\langle \boldsymbol{e}_1 \cdot \boldsymbol{e}_i \rangle = \exp(-s_i/\ell_P)$, where $\boldsymbol{e}_i$ is the unit vector connecting the center of mass positions of particles i and $i + 1$, and s_i is the path length along the polymer to particle i. To implement the persistence length ℓ_P as an input to the simulations, the bending energy is set to $\epsilon_B/(k_B T) = \ell_P/\sigma$ to achieve the desired polymer stiffness. We have set $\ell_P = 3\sigma$ for all of our protein-based simulations based on previous work, and have verified the angular correlation for unbound polymers in 3D as a validation of proper implementation (13).

Sensor particles of different sizes were added to the bulk of the simulation box to model the dynamics of sensor transport and binding to the cell surface. The diameters of the Chol-0.5k PEG, 10k dextran, and 40k dextran sensors were modeled with spheres of diameter 3, 5, and 10 nm, respectively (17). The sensor particles have an attractive potential to the membrane via a Morse potential with the HOOMD parameters ($D_0 = 3 \times 10^9$, $\alpha = 10^{-4}$, $r_0 = \sigma/2$, and $r_{\mathrm{cut}} = \sigma/2 + R$), which effectively approximates a short-range, attractive harmonic potential $U_{\mathrm{att}} = k(z - r_0)^2/2$ with stiffness $k = 2D_0\alpha^2 = 60$. All other particle pairs experience a short-ranged repulsive WCA potential, as described earlier. The dynamics of sensor particle i is evolved in time following the Langevin equation

$$\mathbf{0} = -\zeta_i \boldsymbol{U}_i + \boldsymbol{F}_i^B + \boldsymbol{F}_i^P + \boldsymbol{F}_i^{\mathrm{wall}}, \tag{2.2}$$

where $\boldsymbol{F}_i^{\mathrm{wall}} = \boldsymbol{F}_i^{\mathrm{att}} + \boldsymbol{F}_i^{\mathrm{WCA}}$ is the short-ranged potential that the sensor particle experiences with the surface, $\boldsymbol{F}_i^{\mathrm{att}} = -\nabla U_{\mathrm{att}}$ is the attractive linear force, and $\boldsymbol{F}_i^{\mathrm{WCA}} = -\nabla U_{\mathrm{WCA}}$ is the WCA potential with the surface (see Eqs. 1.14 and 1.15 for definitions of the potentials). In summary, each sensor particle experiences the potentials in Eqs. 1.11 – 1.13 as a function of height z, in addition to the pair-wise WCA potentials with the

protein polymers. It is straightforward to add flexibility and non-spherical shape effects into our sensor model.

Unlike our previous work (13) where a large concentration of passive PEG depletants were added to the bulk to compress the cell surface proteins, in this work we focus on dilute concentrations in which the osmotic compression is negligible. Furthermore, we did not observe any depletion flocculation nor any large-scale protein clustering. Simulations with dilute concentrations of sensors are very time consuming because acquiring sufficient statistics requires many time steps at equilibrium. Therefore, we accelerated our simulations by using a larger concentration of sensor particles that interact only with the protein polymer and the surface, but not with each other. The sensors act as "ideal-gas" particles to each other but interact with WCA potentials with the surface proteins. However, sensor concentrations that are too large can interact with each other indirectly via correlated motion of the protein polymers. A sensor volume fraction less than 1% was used in this work.

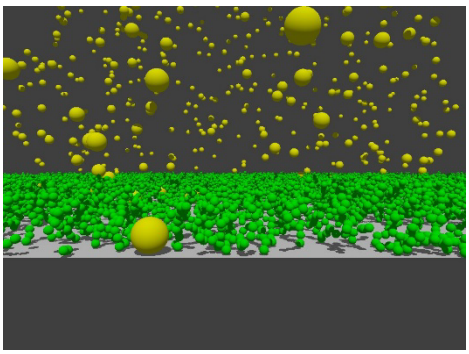

Figure S2.2: Snapshot of coarse-grained MD simulations with sensors (yellow particles) of size $R = 2\sigma$, and surface polymers (green particles) of length $L = 10\sigma$, where σ is the size of an individual monomer.

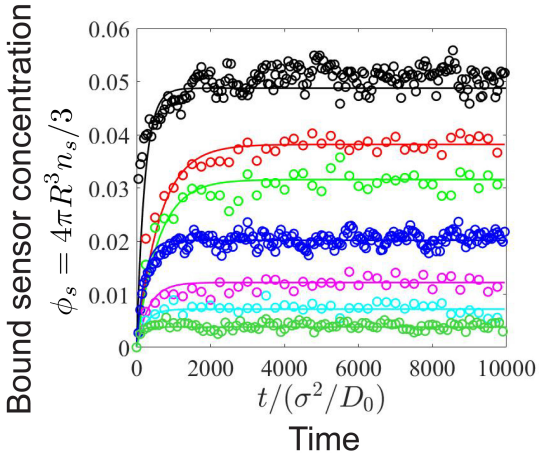

Figure S2.3: Volume fraction of sensors of size $R = \sigma$ on the membrane surface, $\phi_s = 4\pi R^3 n_s/3$, as a function of nondimensional time $t/(\sigma^2/D_0)$, where D_0 is the Stokes-Einstein-Sutherland diffusivity based on the monomer size σ. Solid curves are a fit to a first-order kinetic rate law, ϕ_s/ϕ_s^∞=1 - exp(-t/τ).

We used a system box size of $V = L^2 L_z$, where L was adjusted to achieve the specified area density and number of polymer chains, and L_z was chosen to be sufficiently large to maintain a uniform bath concentration of sensors in the bulk. Dilute surface densities were conducted with ~ 200 chains/μm^2, and the dense surfaces contained ~ 20,000 chains/μm^2. We imposed periodic boundary conditions in the x and y directions, and no-flux hard walls at $z = 0$ and $z = L_z$ to prevent any particles from passing through. Initial configurations were generated by placing the particles in lattice locations, and sufficient time steps were run to reach a steady-state. Time steps were varied from $\Delta t = 10^{-6} - 10^{-4}$ and verified to be sufficiently small to capture relevant dynamics.

A snapshot of the simulations is shown in Fig. S2.2. Simulations were conducted for long enough time steps to sample equilibrium properties. Figure S2.3 shows the concentration of sensors on the membrane surface as a function of time, and we can see that sufficient configurations are sampled after equilibrium is achieved.

2. Calculation of mechanical stress (and pressure) of cell surface proteins

The pressure of cell surface proteins is given by the negative trace of the virial stress tensor,

$$\boldsymbol{\sigma} = -nk_BT\boldsymbol{I} - \frac{1}{V}\langle\sum_i\sum_{j>i}\boldsymbol{r}_{ij}\boldsymbol{F}_{ij}^{P}\rangle, \tag{2.3}$$

where $V = L^2\langle h\rangle$ is the volume of the polymer brush, L is the length of the simulation box, $\langle h\rangle$ is the average height of the polymer surface, $\boldsymbol{r}_{ij}$ is the interparticle distance, and $\boldsymbol{F}_{ij}^{P}$ is the pair-wise interparticle force between all particles, including individual monomers within a single polymer. The first term in Eq. 2.3 is the ideal-gas stress and the number density is defined as $n = N/V$ where N is the total number of particles. The second term is the Irving-Kirkwood virial stress tensor that measures the contribution from interparticle interactions. For polymers, it is important to note that the ideal-gas pressure is $\Pi^{ig} = n_c k_B T$ and not nk_BT, where n_c is the number density of chains, $n_c = N_c/V$ (N_c is the total number of chains). Particles lose their translational degree of freedom when constrained as a polymer, so the ideal-gas pressure decreases with increasing degree of polymerization. Returning to our virial EOS in Eq. 1.6, we can rewrite the ideal-gas expression as $\Pi^{ig} = (k_BT/V_p)\phi/N_R$, where the degree of polymerization $N_R = N/N_c$. For very large molecular weight polymers ($N_R \to \infty$), the ideal-gas contribution is zero and the first term contributing to the osmotic pressure is two-body interactions (i.e., second virial coefficient).

In calculating the osmotic pressure using Eq. 2.3, it would seem like we are overestimating the pressure based on the first term, which assumes that all N particles are independent. However, the virial stress term will cancel the "excess" stress contribution from the nk_BT term. That is, the FENE potential applied to the constitutive particles on the polymers (which represent elasticity) has the opposite sign and subtracts the independent degrees of freedom. The net result is that we correctly recover the ideal-gas pressure of a polymer, $\Pi^{ig} = (k_BT/V_p)\varphi/N_R$.

3. Calculation of free energy potentials

The free energy experienced by the sensor particle as a function of the distance from the membrane surface is given by $U = -k_BT \ln P(z)$, where $P(z)$ is the normalized probability distribution of the sensors. We calculate $P(z)$ by binning the simulation into thin slabs and ensemble averaging over all particles and time. From these distributions, we calculate the effective binding energy and the insertion penalty at equilibrium, as shown in Fig. S2.4. The offset at the energy minimum gives the glycocalyx contribution U_g and the in-plane osmotic pressure of the cell surface.

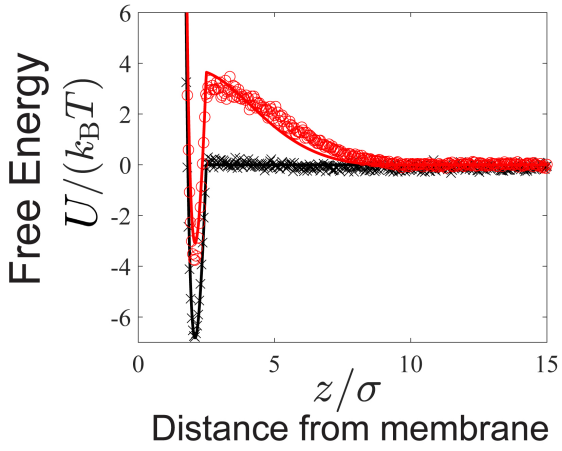

Figure S2.4: Effective free energy potential experienced by a macromolecule of size $R = \sigma$ approaching a bare (black) and crowded (red) cell surface membrane, which is a superposition of two contributions, U_0 and ΔU. The circle and cross symbols are a direct calculation of the free energy via $U = -k_BT \ln P(z)$ from MD simulations, where $P(z)$ is the normalized probability distribution of the sensors. Solid curves are Eqs. 1.17-1.20. The depth of the minimum gives the effective binding energy at equilibrium.

As shown in Fig. S2.4, our analytical theory in Eqs. 1.17-1.20 agrees very well with the direct energy calculations from MD simulations. Once the sensor-substrate affinity is determined in the theory by fitting to the bare-membrane simulations (black symbols and curve), there are no fitting parameters for the crowded surface simulations and theory (red symbols and curve).

4. Incorporation of charges on protein polymers

Charge effects were analyzed in MD simulations by adding a screened coulomb (Yukawa) pair potential between the constituent monomers of the polymer. The energy scale was set to $\epsilon = k_{\mathrm{B}}T$, and the Debye length was varied from $\kappa^{-1} = \sigma$ to $\kappa^{-1} = 2\sigma$. Electrostatic interactions were not included for sensor-polymer or sensor-sensor interactions.

Chapter III. Experimental details

1. Binding isotherms for dextran sensors

In the main text, we obtained the relative difference between the crowded and bare surfaces by taking the ratio of the slopes of the bound sensors at small bulk sensor concentrations. This provides a direct measurement of the relative difference, K_D/K_D^0 (or K_D/K_D^{proK} for RBCs), assuming that the bound saturation concentration, C_{max}, is equal on the crowded and bare surfaces. As a control, we performed a measurement of the effective dissociation constant of the dextran sensors by obtaining the full isotherm across a larger range of bulk concentrations. The maximum saturating concentrations of the sensors, C_{max}, were obtained by incubating the beads and RBCs with 0.5 μM bulk sensor concentration. The bound sensor concentrations at each bulk sensor concentrations were normalized by the maximum concentration at saturation to obtain the fractional surface coverage, $\theta = C/C_{\mathrm{max}}$. The slope at small bulk concentrations were used to obtain the dissociation constant. A representative dataset containing the full isotherm on RBCs for the dextran 40k sensor is shown in Fig. S3.1. The relative ratios of the binding affinities were $K_D/K_D^{\mathrm{proK}} = 1.5$ and 2.6 for sialidase-treated and untreated RBCs, respectively, which agree with the results in the main text obtained using a ratio of the slopes at small bulk concentrations.

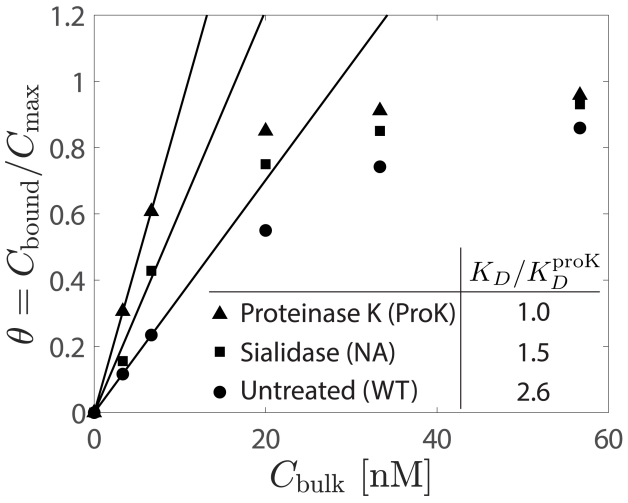

Figure S3.1. Surface coverage of bound 40k dextran sensors as a function of bulk concentration of sensors on untreated (circle), sialidase (NA)-treated (square), and Proteinase K-treated (triangle) RBCs. Each measurement was normalized by the maximum concentration at saturation to obtain the fractional surface coverage, $\theta = C/C_{\mathrm{max}}$. The slope at small bulk concentrations, shown as solid lines, were used to obtain the dissociation constant.

2. Effective dissociation constants of multivalent binding species

As shown by Cremer et al. (18,19), interpretation of the effective dissociation constant of multivalent binding species requires some care. For bivalent-binding antibodies, there are two dissociation constants, K_{D1} and K_{D2}, defined by $K_{D1} = [A][L]_s/[AL]_s$ for the first binding event, and $K_{D2} = [AL]_s[L]_s/[AL_2]_s$ for the second binding when both binding sites are bound to the two ligands. The total surface concentration of sites is $[L]_s/2 + [AL]_s/2 + [AL_2]_s$, so the fraction of bound species is

$$\theta = \frac{\text{total bound antibodies}}{\text{total number of sites}} = \frac{[AL]_s + [AL_2]_s}{[L]_s/2 + [AL]_s/2 + [AL_2]_s} = \frac{\alpha[A]}{K_D + [A]}$$

where $\alpha = (K_{D2} + [L]_s)/(K_{D2} + 2[L]_s)$ is a number that varies between 0.5 and 1.0, and the effective dissociation constant is given by

$$K_D = \frac{K_{D1}K_{D2}}{K_{D2} + 2[L]_s}$$

Therefore, the binding isotherm still takes on the classic Langmuir form, except the interpretation of the effective K_D is slightly different. At small bulk antibody concentrations, $[A] \ll 1$, we are still fitting a line with the slope that gives the effective dissociation constant. The main potential issue is that the effective dissociation constant is now a function of the ligand concentration, $[L]_s$. This is not an issue for our dextran-based sensors because the "ligand" concentration is simply the total available surface area on the beads and cells, which is fixed constant in each respective experiment.

However, this is a potential issue for our antibody-based measurement because our biotin-DNA cholesterol sensors incorporate into cell membranes with different affinities. Therefore, the ligand concentration $[L]_s$ could be changing drastically as a function of cell type, over-expression, etc. As shown in the expressions above, varying $[L]_s$ will change the effective dissociation constants, which is an unwanted problem. In fact, we did indeed see this effect when we used a very large concentration of the biotin-based cholesterol sensors.

This issue has been addressed previously by Yang et al (19), in which they observed a 10x decrease in effective K_D of monoclonal antibodies on SLB-coated beads when the ligand surface density was increased from 1400/μm^2 to 40,000/μm^2. Fortunately, they found that the effective K_D increased only from $13\mu M$ to $18\mu M$ when increasing the ligand surface density from 1400/μm^2 to 4200/μm^2 (small ligand concentrations). We therefore hypothesized that staying at small surface ligand concentrations would reduce or eliminate this potential uncertainty of determining the effective K_D.

To these ends, we performed control experiments with varying amounts of biotin-based cholesterol sensors on beads, RBCs, and mammalian cells. We found that the effective dissociation constant was insensitive to changes in $[L]_s$ when $[L]_s \ll 1$. In other words, the parameters α and K_D above were not a function of $[L]_s$ at the low ligand concentrations used in our measurements.

The rationale for this result in the context of the equations above is that $\lim_{[L]_s \to 0} \alpha \to 1$ and $\lim_{[L]_s \to 0} K_D \to K_{D1}$. In other words, we are measuring essentially the monomeric binding affinity of the antibody because the surface ligand concentration is so low, and the second binding constant K_{D2} drops out of the problem. Therefore, our approach to obtain the effective dissociation constant from the Langmuir isotherm form is an appropriate way to obtain the binding affinities and energies, and our results are insensitive to the absolute surface concentrations of the ligand sensors.

3. Sensors have no non-specific adsorption onto membranes

Our dextran sensors have a strong affinity to insert into the lipid bilayer via cholesterol tags bound to the dextran molecules. To rule out the possibility of other, non-specific interactions of the dextran sensors onto membranes, we conjugated the dextran molecules to Alexa Fluor dyes only, without cholesterol tags. Upon incubating these dextran-dye sensors with lipid-coated beads and red blood cells (RBCs), we did not detect

enrichment on the membrane, validating that the main adsorption mechanism of our sensors is via the cholesterol tags. A representative microscopy image is shown in Fig. S3.2. We conclude that there is a negligibly small adsorption and non-specific interaction of our dextran macromolecules with the membrane. For our other probe based on anti-biotin binding, an antibody-only control was performed on cholesterol anchors containing no biotin tag (a cholesterol-FITC construct), and we observed no nonspecific anti-biotin binding on the membrane.

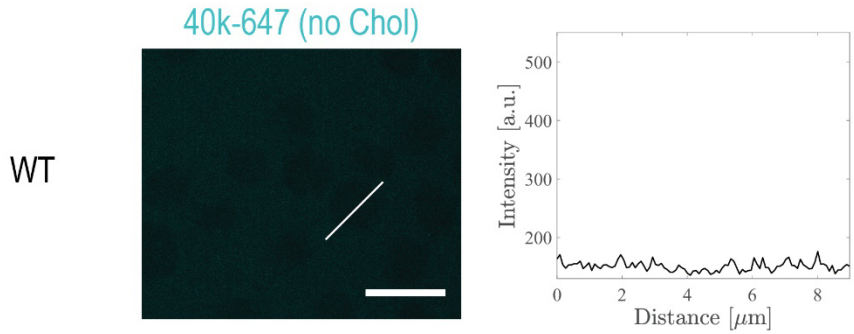

Figure S3.2. There is no non-specific adsorption of our sensors onto membranes. Dextran-dye sensors in the absence of cholesterol does not incorporate into lipid coated beads or RBC membranes.

4. Control experiments of dextran sensors with different chemistries.

In the previous section, we showed that the intrinsic dextran macromolecules (without cholesterol) do not exhibit non-specific adsorption onto the membrane. However, the Alexa Fluor dyes conjugated to the cholesterol-dextran macromolecules are negatively charged and may interact electrostatically with the charged cell surface. As a control, we conjugated our cholesterol-dextran sensors with BODIPY, a charge-neutral dye. As shown in the main text, RBCs have highly charged cell surfaces that we can modulate using neuraminidase (NA) treatment; RBCs are a good model system to examine the interactions between the cell surface and the sensor dye charges.

We conducted two tests on RBCs to assess the impact of the dye charges. First, to test whether the binding kinetics are equivalent between the Alexa Fluor and BODIPY conjugated cholesterol-dextran sensors, we took a time series of sensor binding on untreated and neuraminidase (NA) treated RBCs. As shown in Fig. S3.3, the binding kinetics of both dye types are essentially identical across the RBC surfaces. Note that the important feature from Fig. S3.3 is the time constant towards equilibrium, not the final saturation value. The final equilibrium value is irrelevant because the intensity units from the flow cytometer is different across the two different laser channels, and because the two sensor types may contain a slightly different labeling ratio of cholesterol. The dashed and solid curves in Fig. S3.3 are a fit to a first-order kinetic rate law, $C/C_\infty = 1 - \exp(-t/\tau)$. The characteristic decay time towards equilibrium is τ = 7.53 min (WT) and τ = 7.05 min (NA) for the Alexa Fluor 647 conjugated dextran sensors and τ = 7.38 min (WT) and τ = 7.51 min (NA) for the BODIPY conjugated dextran sensors. All of these values are similar to each other, which validates that the binding kinetics between the charged Alexa Fluor dyes and neutral BODIPY dyes have no difference. Within the same dye, the fact that the binding kinetics are the same between the WT cells (fully charged) and NA-treated cells (reduced charge) is another indication that the kinetics are unaffected by cell surface charges.

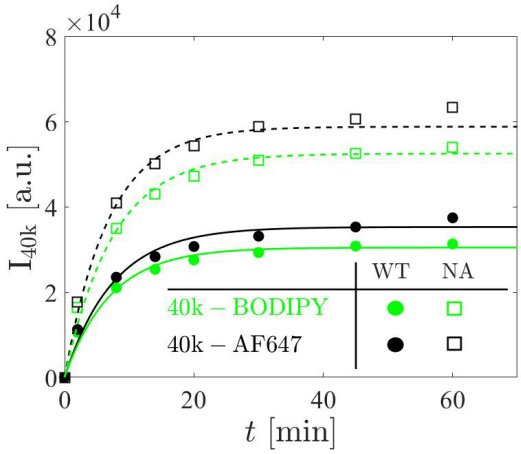

Figure S3.3. Bound sensor concentration as a function of time for Alexa Fluor 647 conjugated dextran sensors (black curves and symbols) and BODIPY conjugated dextran sensors (green curves and symbols), on untreated RBCs ("WT", filled circle symbols) and NA-treated RBCs ("NA", open square symbols). Solid and dashed curves are a fit to a first-order kinetic rate law, C/C_∞ = 1 - exp(-t/τ). The characteristic decay time towards equilibrium is τ = 7.53 min (WT) and τ = 7.05 min (NA) for the Alexa Fluor 647 conjugated dextran sensors and τ = 7.38 min (WT) and τ = 7.51 min (NA) for the BODIPY conjugated dextran sensors. This validates that the binding kinetics between the charged Alexa Fluor dyes and neutral BODIPY dyes has no difference.

Next, we tested whether the effective dissociation constant K_D is different between the Alexa Fluor and BODIPY conjugated cholesterol-dextran sensors. As described in the main text, we performed an equilibrium measurement of sensor binding on untreated and NA-treated RBCs using both types of sensors. The binding measurement at large bulk concentrations provide the saturating binding concentration, C_max, and the fractional coverage may be obtained using small bulk concentrations, $\theta = C/C_\mathrm{max}$. As presented in the main text, our key metric of comparison is the relative difference between the binding affinities of WT and NA-treated cells, not the absolute value of K_D. As shown in Fig. S3.4, we find that the ratio of the binding affinities on NA-treated and WT RBCs are $K_\mathrm{D}^{NA}/K_\mathrm{D}^{WT} = 0.634$ for BODIPY conjugated cholesterol-dextran and $K_\mathrm{D}^{NA}/K_\mathrm{D}^{WT} = 0.652$ for Alexa Fluor 647 conjugated cholesterol-dextran. This validates that the negative charges on the Alexa Fluor 647 dyes do not impact the results presented in Fig. 2 of the main text.

We believe that the negative charges on the dextran sensors play a small role for our particular system in part because the bound sensor concentrations are very dilute on the RBC surface. The average separation distance between the dextran sensors on the RBC surface over the range of interest is $\approx$ 100 nm at 100/μm^2 surface density, and the average distance between the dextran sensors and the GYPA proteins is $\approx$ 10 nm at 2000/μm^2 GYPA surface density. Both of these distances are more than an order of magnitude larger than the small 0.7 nm Debye length in physiological buffers, so we expect that the majority of the charge interactions are screened. Interestingly, the absolute magnitudes (not the ratio) of K_D for the BODIPY sensors are larger than the Alexa Fluor sensors, which is the opposite of what one may expect based on electrostatic repulsion between the dye and the charged cell surface. One may naively expect that the negative charge repulsion between the Alexa Fluor and the RBC surface would cause less binding and a larger K_D for the Alexa Fluor sensors. At very large sensor concentrations, the surface is saturated with a dense packing of sensors. Here, we believe that the average separation distance between neighboring sensors may be similar to the Debye length, and the negative charge repulsion among the neighboring sensors' Alexa Fluor dyes may lead to smaller packing and a smaller C_max than the BODIPY conjugated dextran sensors. A smaller saturating concentration would normalize the fractional coverage to a larger value, leading to smaller absolute magnitude of K_D for the Alex Fluor conjugated dextran sensors. In summary, the effects of negative charges on the dye do not impact the normalized ratio of the binding affinities at the dilute concentrations that form the basis of our crowding measurements; however, they are

an important consideration in general when the absolute magnitudes of K_D are desired or one would like to use these sensors at much larger concentrations.

Once again, the absolute magnitudes of K_D are unimportant for our work because we are only interested in relative ratios between the different cell treatments. The crowding free energies come from the ratio in the binding affinity on bare and crowded surfaces, $\Delta U = k_B T \ln(K_D/K_D^0)$, not the absolute magnitude. The absolute magnitudes for the dextran sensors depend on the intrinsic chemistries of the cholesterol interaction with the membrane, which is irrelevant for our crowding measurements.

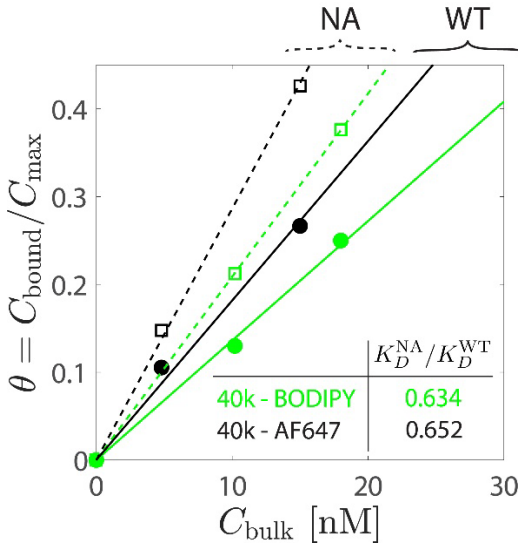

Figure S3.4. Surface coverage of bound 40k dextran sensors as a function of bulk concentration of Alexa Fluor 647 conjugated dextran sensors (black lines and symbols) and BODIPY conjugated dextran sensors (green lines and symbols), on untreated RBCs ("WT", filled circle symbols) and NA-treated RBCs ("NA", open square symbols). Solid and dashed lines are a fit to obtain the dissociation constant. We find that the ratio of the binding affinities on NA-treated and WT RBCs are $K_D^{NA}/K_D^{WT} = 0.634$ for BODIPY conjugated cholesterol-dextran and $K_D^{NA}/K_D^{WT} = 0.652$ for Alexa Fluor 647 conjugated cholesterol-dextran. This validates that the negative charges on the Alexa Fluor 647 dyes do not impact the results presented in Fig. 2 of the main text.

5. Verification that the stock sialidase is protease-free.

A sodium dodecyl sulfate polyacrylamide gel electrophoresis (SDS-PAGE) protein gel of bovine serum albumin (BSA), MW = 66 kDa, is shown in Fig. S3.5. BSA was treated with various concentrations of sialidase and Proteinase K at 37C for 5 hours. The protein was subsequently heat-denatured in 1x Laemmli Sample Buffer (Sigma Aldrich) in the presence of β-mercaptoethanol. The sample was then loaded onto a NuPAGE Novex 4–12% gradient Bis-Tris gel (Fisher Scientific) and separated by electrophoresis. This gel confirms that our stock sialidase does not have protease activity. In addition to BSA, we collected the supernatant of RBCs treated with sialidase and found no detectable signal of proteins released from the RBC surface as a result of sialidase treatment. This verifies that soluble sialic acid-binding proteins are not embedded in the glycocalyx to hinder the binding of the sensors.

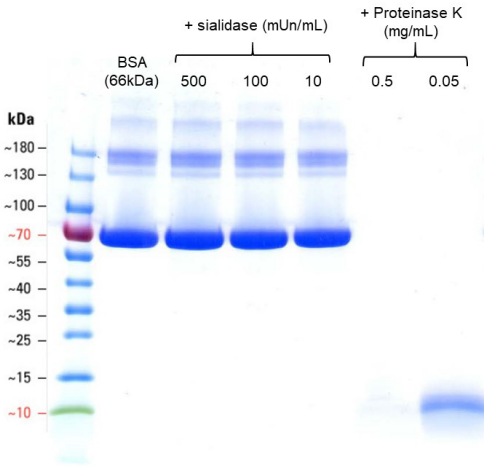

Figure S3.5. Sodium dodecyl sulfate polyacrylamide gel electrophoresis (SDS-PAGE) protein gel of bovine serum albumin (BSA), MW = 66 kDa, treated with enzymes sialidase and Proteinase K at 37C for 5 hours. We detected no protease activity in our stock sialidase. In our experiments, RBCs were treated with sialidase at 50 mUn/mL.

6. EDC conjugation to remove negative charges from cell surface

We used a carbodiimide crosslinker chemistry based on 1-Ethyl-3-(3-dimethylaminopropyl)carbodiimide (EDC) to remove negative charges present on carboxylic acid groups on the red blood cell surface. Most surface negative charges come from the carboxylic acid on the sialic acids, but charged amino acids (e.g., aspartic acid and glutamic acid) may also be impacted by this reaction. We added EDC and hydrazide-biotin (a charge-neutral molecule) to a suspension of red blood cells, and the effectiveness of the reaction was assessed by imaging with AF555-labeled straptavidin. As shown in Fig. S3.6, the reaction was qualitatively very effective and we believe that most negative charges were neutralized on the cell surface.

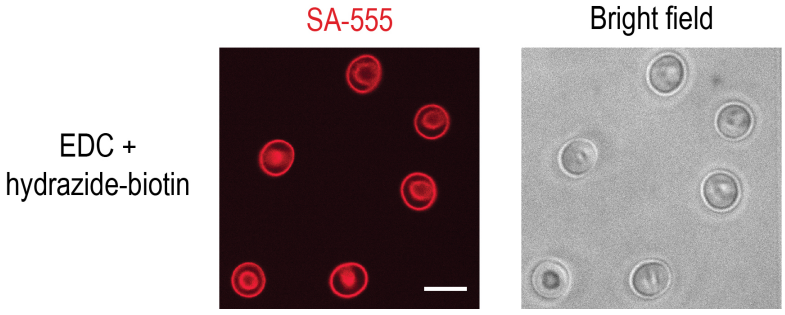

Figure S3.6. EDC chemistry was used to remove negative charges from the red blood cell surface. The reaction conjugated hydrazide-biotin to carboxylic acid sites, which enabled detection using AF555-labeled streptavidin to image the red blood cell surface. Scalebar is 10 μm.

7. Sensor internalization in mammalian cells is minimal when performed on ice.

To prevent internalization of the macromolecules into the mammalian cell interior, the cells were incubated on ice throughout the measurement. We confirmed using confocal microscopy that the majority of the sensors are localized on the cell surface and appear to be bound homogeneously, as shown in Fig. S3.7. In Fig S3.7, the sensors were not added at the same concentration to test for robustness against internalization across a wide range of sensor concentrations. In all of our reported measurements, we did not observe significant internalization of neither the biotin anchor nor the antibody when performing the experiments on ice.

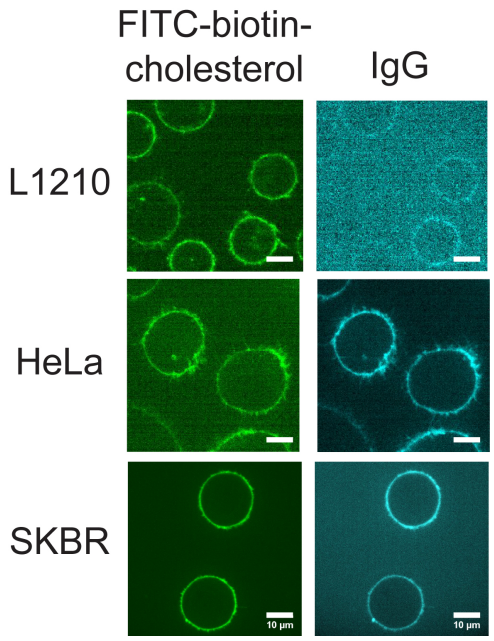

Figure S3.7. Representative confocal images of three cancer cell types incubated with biotin-FITC-cholesterol construct (left) and surface-bound IgG (right). Majority of the signal is localized on the cell surface. This is a test to check for sensor internalization, so these images do not correspond to the same sensor concentrations and the arbitrary image intensity is not reflective of the crowding state of the cells. All scale bars are 10 μm.

8. Bound antibody concentration normalized by the bound biotin-FITC-cholesterol concentration is independent of heterogeneities in cell size.

The advantage of using the DNA-based FITC-biotin-cholesterol sensor is that this construct acts as a proxy of cell size and cell membrane surface area. A plot of normalized bound antibody signal (i.e., antibody intensity divided by the FITC intensity) as a function of forward scattering (a metric of cell size) is shown in Fig. S3.8. We observe a constant normalized bound antibody across a 6x change in forward scattering, which indicates that the variations in cell membrane area is properly accounted for in our calculation of cell heterogeneities. By obtaining the fraction of bound antibodies by dividing against the FITC signal, we are normalizing for cell heterogeneities in shape and surface area. This normalization enables a measurement of population heterogeneities within a sample, which we cannot do using the dextran sensors.

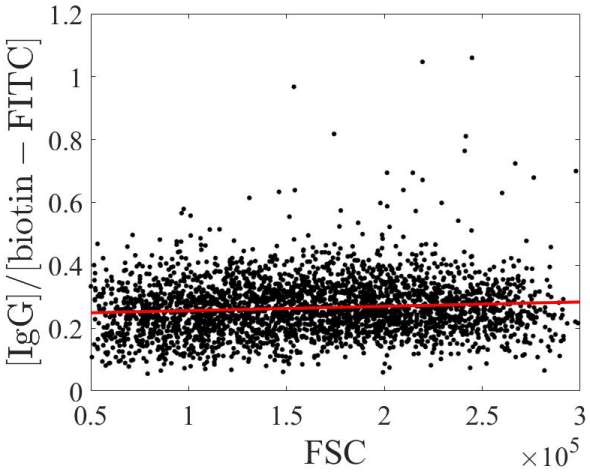

Figure S3.8. Representative flow cytometry data for HeLa cells of normalized antibody signal as a function of forward scatter. Black dots are individual cells and the red line is a linear fit to the data. We obtain approximately zero slope in the linear fit, which indicates that the normalized antibody concentration is independent of cell size.

Chapter IV. Additional supplemental figures

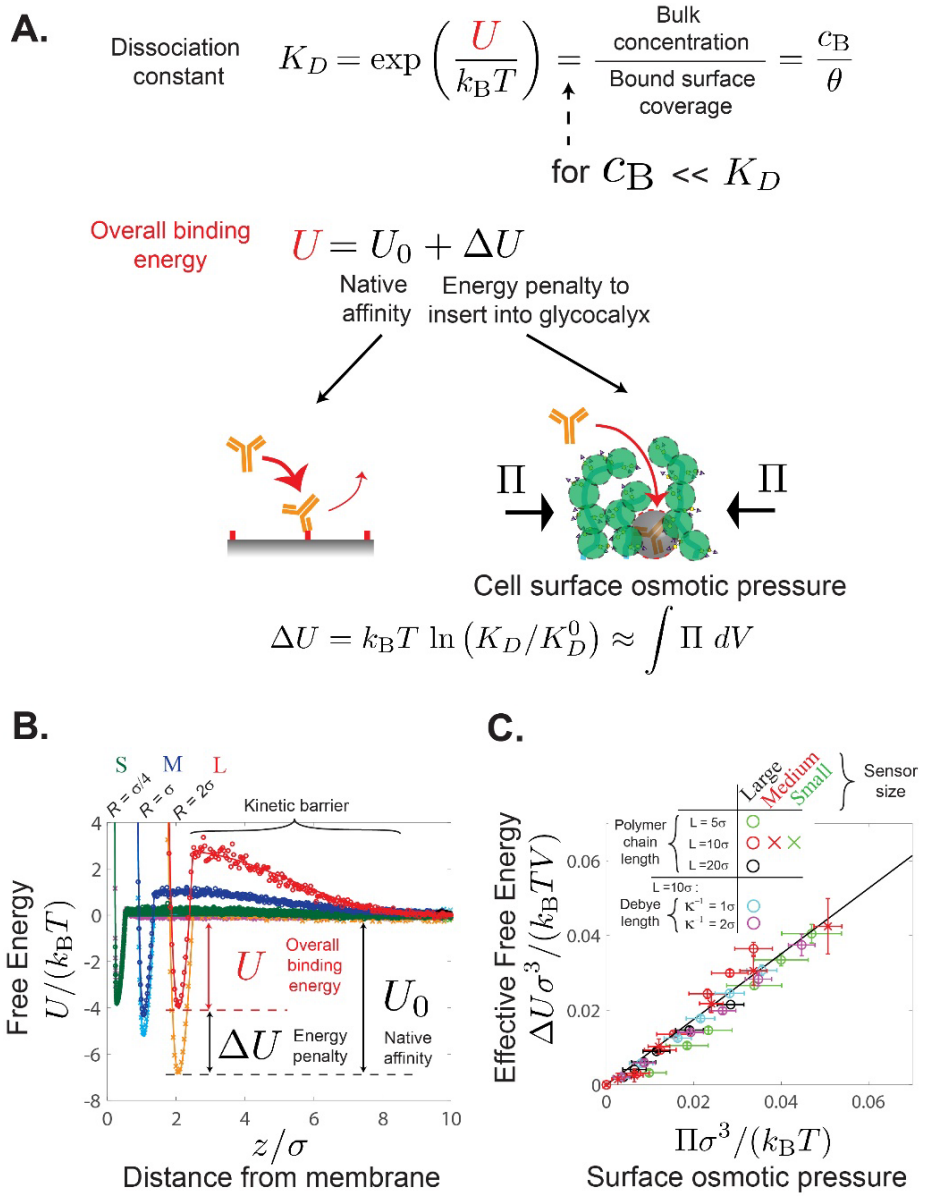

Figure S4.1. Macromolecular crowding on membrane surfaces is described by a surface osmotic pressure.

(A) The dissociation constant of a surface-binding macromolecule is given by its binding energy, U, which is a sum of the intrinsic affinity, U_0, and the penalty due to crowding, ΔU. The energy penalty posed by surface crowding is directly related to the change in normalized binding affinity, K_D/K_D^0, and the osmotic pressure of the surface, Π.

(B) Coarse-grained molecular dynamics (MD) simulations were used to calculate the binding energy curves for spherical sensors of sizes $\sigma_s = 0.25\sigma$ (small), σ (medium), and 2σ (large), where σ is the coarse-grained effective diameter of a glycocalyx polymer chain. The depth of the minimum gives the effective binding energy at equilibrium. The surface contains polymers with contour length 10σ at a concentration of $\sim 10{,}000/\mu m^2$.

(C) The energy penalty across various sensor sizes, surface polymer lengths, and surface polymer charges all collapse onto a unifying scaling line when the data are plotted against the osmotic pressure generated by the surface polymers, Π. The multi-domain proteins on the surface have varying lengths and are either charged (cyan and magenta circles) or neutral (all other symbols). Electrostatic interactions among the polymers are modeled by a Yukawa potential with different Debye lengths, κ^{-1}. The energy penalty ΔU is normalized by the effective volume of the sensor immersed inside the crowded surface, V, and Π is calculated via the Irving-Kirkwood virial stress tensor. Error bar indicates standard deviations of ensembles over all time and particles. The solid line is given by analytical theory and is not a fit.

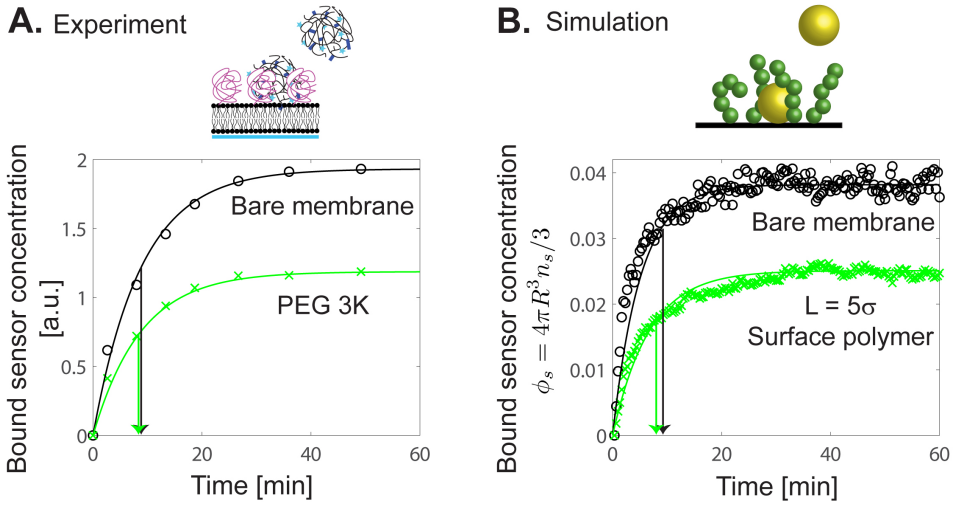

Figure S4.2. Sensor binding on crowded membrane surfaces approaches equilibrium at similar rates for bare and crowded surfaces.

(A) Bound dextran-40k sensor concentration as a function of time on bare membrane beads (black symbols) and crowded PEG 3K surfaces (green symbols) saturates with the same time constant. Solid curves are a fit to a first-order kinetic rate law, C/C_∞ = 1 - exp(-t/τ). The characteristic decay time towards equilibrium is τ = 8.86 min for bare membranes and τ = 8.74 min for crowded PEG 3K surfaces.

(B) MD simulations of sensor binding on bare surfaces (black symbols) and crowded surfaces (green symbols), where $\phi_s = 4\pi R^3 n_s/3$ is the volume fraction of bound sensors at the surface. The characteristic decay time towards equilibrium is τ = 9.8 min for bare membranes and τ = 9.0 min for crowded polymer surfaces.

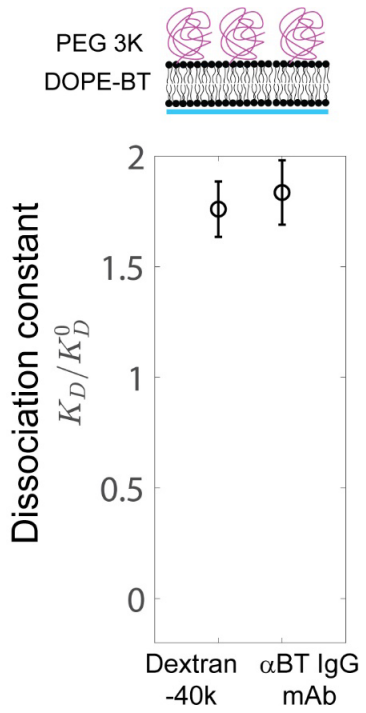

Figure S4.3. The crowding penalties reported by the large dextran-40k sensor and anti-biotin IgG antibodies are quantitatively similar on crowded reconstituted surfaces, consistent with their similar size (~10 nm).

We confirmed that our alternative measurement using antibodies provides a readout of crowding consistent with the dextran-40k sensor.

Experimental materials and resources

Purified human Glycophorin A (CD235a) extracellular domain with a C-terminal 6x-His tag (catalog number: 16018-H08H) was purchased from Sino Biological US Inc.
Alexa Fluor 647 labeled anti-biotin (BK-1/39; catalog number: sc-53179 AF647) was purchased from Santa Cruz Biotechnology. Monoclonal antibodies against human Glycophorin AB (CD235ab) (HIR2; catalog number: 306602) and human CD47 (CC2C6; catalog number: 323102) were purchased from BioLegend.

BD Microtainer Contact Activated Lancet, 30 G x 1.5 mm, low flow, purple (catalog number: 366592) was purchased from BD Biosciences.

Lectins Sambucus Nigra Lectin (SNA; catalog number: L-1300), Fluorescein labeled Agaricus bisporus lectin (ABL; catalog number: FL-1421), Fluorescein labeled Erythrina cristagalli lectin (ECL; catalog number: FL-1141), and Wheat Germ Agglutinin (WGA; catalog number: L-1020-10) were purchased from Vector Laboratories.

1,2-dioleoyl-sn-glycero-3-(N-(5-amino-1-carboxypentyl)iminodiacetic acid)succinyl (DGS-Ni-NTA; catalog number: 709404), 1,2-dioleoyl-sn-glycero-3-phosphocholine (DOPC; catalog number: 850375), 1,2-dioleoyl-sn-glycero-3-phospho-L-serine (DOPS; catalog number: 840035), 1,2-dioleoyl-sn-glycero-3-phosphoethanolamine-N-(cap biotinyl) (Biotinyl Cap PE; catalog number: 870273), 1,2-dioleoyl-sn-glycero-3-phosphoethanolamine-N-methoxy(polyethylene glycol)-2000 (PEG2k PE; catalog number: 880130), 1,2-dioleoyl-sn-glycero-3-phosphoethanolamine-N-methoxy(polyethylene glycol)-3000 (PEG3k PE; catalog number: 880330) were purchased from Avanti polar lipids.

Silica microspheres (4.07μm; catalog code: SS05002; lot number: 12602 and 6.84μm; catalog code: SS06N; lot number: 4907) were purchased from Bangs laboratories. Cholesterol NHS (catalog number: CSL02) was purchased from Nanocs Inc. Cholesterol-PEG-Amine, MW 1k (catalog number: PLS-9961) was purchased from Creative PEGWorks. Dextran, Amino, 10,000 MW (10k dextran; catalog number: D1860), Dextran, Amino, 40,000 MW (40k dextran; catalog number: D1861), Alexa Fluor 647 NHS Ester (Succinimidyl Ester) (NHS-AF647; catalog number: A20006), Alexa Fluor 555 NHS Ester (Succinimidyl Ester) (NHS-AF555; catalog number: A20009), Alexa Fluor 488 NHS Ester (Succinimidyl Ester) (NHS-AF488; catalog number: A20000) , BODIPY FL NHS Ester (Succinimidyl Ester) (NHS-BODIPY; catalog number: D2184) were purchased from Invitrogen.

NHS-Fluorescein (5/6-carboxyfluorescein succinimidyl ester) (NHS-FITC; catalog number: 46409), DyLight 650-4xPEG NHS Ester (catalog number: 62274), EZ-Link Hydrazide-Biotin (hydrazide-biotin; catalog number: 21339), EDC (1-ethyl-3-(3-dimethylaminopropyl)carbodiimide hydrochloride) (catalog number: 77149), Zeba Spin Desalting Column, 7K MWCO (catalog number: 89882) were purchased from Thermo Scientific.

Proteinase K from Tritirachium album (catalog number: P2308) and sialidase from Clostridium perfringens (C. welchii) (catalog number: N2876) were purchased from Sigma. FITC-biotin-DNA-cholesterol construct (5'-FITC-TTTTTT-biotin-TTT-cholesterol-3') was purchased from Integrated DNA Technologies, Inc.

MATLAB educational license was obtained from MathWorks Inc. UC Berkeley's BRC High Performance Computing Savio cluster with NVIDIA K80 GPU were used for molecular simulations. Attune NxT Acoustic Focusing Cytometer (ThermoFisher Scientific) was used for all of the flow cytometer experiments.

References

1 Doi, M. *Soft matter physics*. (Oxford University Press, 2013).

2 Hall, D. & Minton, A. P. Macromolecular crowding: Qualitative and semiquantitative successes, quantitative challenges. *Biochimica et Biophysica Acta (BBA) - Proteins and Proteomics* **1649**, 127-139 (2003).

3 Kim, J. S. & Yethiraj, A. Effect of macromolecular crowding on reaction rates: A computational and theoretical study. *Biophys J* **96**, 1333-1340 (2009).

4 Minton, A. P. Effective hard particle model for the osmotic pressure of highly concentrated binary protein solutions. *Biophys J* **94**, L57-L59 (2008).

5 Stachowiak, J. C., Schmid, E. M., Ryan, C. J., Ann, H. S., Sasaki, D. Y., Sherman, M. B., Geissler, P. L., Fletcher, D. A. & Hayden, C. C. Membrane bending by protein–protein crowding. *Nature Cell Biology* **14**, 944-949 (2012).

6 Rubinstein, M. & Colby, R. H. *Polymer physics*. (OUP Oxford, 2003).

7 Halperin, A. Polymer brushes that resist adsorption of model proteins: Design parameters. *Langmuir* **15**, 2525-2533 (1999).

8 Halperin, A., Fragneto, G., Schollier, A. & Sferrazza, M. Primary versus ternary adsorption of proteins onto peg brushes. *Langmuir* **23**, 10603-10617 (2007).

9 Halperin, A. & Zhulina, E. B. Atomic force microscopy of polymer brushes: Colloidal versus sharp tips. *Langmuir* **26**, 8933-8940 (2010).

10 Louis, A. A., Bolhuis, P. G., Meijer, E. J. & Hansen, J. P. Density profiles and surface tension of polymers near colloidal surfaces. *The Journal of Chemical Physics* **116**, 10547-10556 (2002).

11 Weeks, J. D., Chandler, D. & Andersen, H. C. Role of repulsive forces in determining the equilibrium structure of simple liquids. *Journal of Chemical Physics* **54**, 5237-5247 (1971).

12 Milner, S. T., Witten, T. A. & Cates, M. E. Theory of the grafted polymer brush. *Macromolecules* **21**, 2610-2619 (1988).

13 Son, S., Takatori, S. C., Belardi, B., Podolski, M., Bakalar, M. H. & Fletcher, D. A. Molecular height measurement by cell surface optical profilometry (csop). *Proceedings of the National Academy of Sciences* **117**, 14209-14219 (2020).

14 Kremer, K. & Grest, G. S. Molecular dynamics (md) simulations for polymers. *Journal of Physics: Condensed Matter* **2**, SA295-SA298 (1990).

15 Anderson, J. A., Lorenz, C. D. & Travesset, A. General purpose molecular dynamics simulations fully implemented on graphics processing units. *Journal of Computational Physics* **227**, 5342-5359 (2008).

16 Glaser, J., Nguyen, T. D., Anderson, J. A., Lui, P., Spiga, F., Millan, J. A., Morse, D. C. & Glotzer, S. C. Strong scaling of general-purpose molecular dynamics simulations on gpus. *Computer Physics Communications* **192**, 97-107 (2015).

17 Armstrong, J. K., Wenby, R. B., Meiselman, H. J. & Fisher, T. C. The hydrodynamic radii of macromolecules and their effect on red blood cell aggregation. *Biophys J* **87**, 4259-4270 (2004).

18 Jung, H., Yang, T., Lasagna, M. D., Shi, J., Reinhart, G. D. & Cremer, P. S. Impact of hapten presentation on antibody binding at lipid membrane interfaces. *Biophys J* **94**, 3094-3103 (2008).

19 Yang, T., Baryshnikova, O. K., Mao, H., Holden, M. A. & Cremer, P. S. Investigations of bivalent antibody binding on fluid-supported phospholipid membranes: The effect of hapten density. *Journal of the American Chemical Society* **125**, 4779-4784 (2003).